Title: Gβ promotes receptor polarization and chemotropism by inhibiting receptor phosphorylation

Authors: A. Ismael[1], W. Tian[2†], N. Waszczak[1†], X. Wang[1†], Y. Cao[2], D. Suchkov[1✦], Eli Bar[1✧], M. V. Metodiev[3], J. Liang[2], R. Arkowitz[4], and D. E. Stone[1*]

One Sentence Summary: In pheromone-treated yeast cells, Gβ interaction with kinases at the incipient polarized growth site inhibits receptor phosphorylation and promotes its polarization, which contributes to chemotropism.

Affiliations:

[1]Department of Biological Sciences, University of Illinois at Chicago, Chicago, IL 60607, USA.

[2]Department of Bioengineering, University of Illinois at Chicago, Chicago, IL 60607.

[3]School of Biological Sciences, University of Essex, Essex, UK.

[4]CNRS UMR7277 / INSERM UMR1091 / Université de Nice - Sophia Antipolis, Institute of Biology Valrose, Nice, France.

[✦]Cellecta Incorporated, Mountain View, CA 94043.

[✧]Department of Neurological Surgery, Case Western Reserve University, Cleveland, OH 44106.

*Correspondence to: D. S. at the Laboratory for Molecular Biology, Department of Biological Sciences, University of Illinois at Chicago, 900 South Ashland Avenue, Chicago, IL 60607, USA; e-mail: dstone@uic.edu; phone: 312-996-5710; fax: 312-413-2691.

[†]These authors contributed equally to this work.

ABSTRACT

Gradient-directed cell migration and growth are universal processes, essential to the development and life cycles of all species. Cells use surface receptors to sense the shallow chemical gradients that elicit chemotaxis and chemotropism. Slight asymmetries in spatial cues are amplified by downstream signaling systems, which ultimately induce polarization of the cytoskeleton. During the mating response of budding yeast, a model chemotropic system, the pheromone receptor polarizes to the up-gradient side of the cell, but how this happens is unknown. Although receptor polarization occurs prior to and independently of directed secretion, it requires receptor internalization. Casein kinase (Yck1/2)-dependent receptor phosphorylation triggers receptor internalization. Here we show that the pheromone-responsive Gβγ promotes polarization of its receptor by interacting with Yck1/2 and locally inhibiting receptor phosphorylation. We also present evidence that implicates receptor phosphorylation in chemotropism, independent of its role as a trigger for receptor internalization. A mathematical model supports the idea that Gβγ-Yck1/2 interaction results in differential phosphorylation and internalization of the receptor and accounts for its polarization upstream of directed secretion.

INTRODUCTION

Polarized cellular growth in response to a chemical gradient (chemotropism) is a fundamental process required for a broad range of phenomena. These include angiogenesis, axon growth cone guidance, pollen tube guidance, fungal life cycles, and fungal pathogenicity. Like chemotaxing cells, chemotroping cells must be able to determine the direction of dynamic chemical gradients, establish a stable axis of polarity, and realign that axis as they track changes in the gradient.

The ability of the budding yeast, *Saccharomyces cerevisiae*, to mate efficiently depends on what is to date the best understood chemotropic response. During the sexual reproduction phase of their life cycle, haploid yeast cells of opposite mating type, *MAT***a** and *MAT*α, signal their position to one another by secreting peptide pheromones. The binding of pheromone to G protein coupled receptors (GPCRs) on the surface of each cell type, and consequent activation of the cognate heterotrimeric G protein, induces cell cycle arrest, changes in gene expression, and the formation of mating projections, commonly called shmoos. Cells grow up the pheromone concentration gradient toward a potential mating partner, leading to the eventual fusion of the partners at their growth tips (*1*). The polarization of cell growth (morphogenesis) is accomplished by the directed movement of secretory vesicles along actin cables oriented toward the growth site (*2, 3*). The Gβγ subunit of the heterotrimeric G protein serves as a positional determinant for the chemotropic growth site by linking the receptor to the machinery that nucleates actin cables (*4, 5*).

As the most upstream elements in the mating response pathway, the pheromone receptor and its G protein are the primary gradient sensors. Unlike most chemotaxing cells, whose surface receptors are uniformly distributed, pheromone-stimulated yeast cells polarize their GPCR. In response to isotropic pheromone treatment, the receptor concentrates around the predetermined bud site, also known as the default polarity site. In mating mixtures, the receptor polarizes towards proximal mating partners, on the presumptive up-gradient side of the cell, and this phenomenon is detectable prior to morphogenesis (*6*). The phenomenology and regulation of pheromone-induced receptor polarization in *MAT***a** cells is well documented. During vegetative growth, the *MAT***a**-specific receptor, Ste2, appears uniformly distributed on the plasma membrane (PM). When activated by ligand, however, the receptor is sequentially phosphorylated

and ubiquitinated on its C-terminal cytoplasmic domain (*7, 8*). This triggers its global internalization, after which it reappears as a polarized crescent on the cell surface (*9, 10*).

Although receptor polarity could arise from directed delivery of nascent receptors to the incipient shmoo site, several observations argue for a distinct mechanism. First, the Ste2 receptor polarizes prior to morphogenesis. Second, establishment of receptor polarity does not depend on directed vesicle delivery along actin cables (*6*). Third, the genesis of receptor polarity absolutely depends on receptor internalization (*6*).

How does the receptor polarize towards the gradient source prior to and independent of actin-cable directed secretion? One possibility is that the pheromone-induced global internalization of the receptor is slower on the up-gradient side of the cell such that relative receptor density increases at the future shmoo site. This is consistent with the observation that the redistribution of the receptor depends on its internalization, but at the same time, it introduces a paradox: Because only activated receptors are phosphorylated, ubiquitinated and internalized, the rate at which the receptor is removed from the cell surface should be greatest where the pheromone concentration is highest. In principle, therefore, the establishment of the chemotropic growth site via differential internalization of the receptor requires a mechanism to locally inhibit receptor internalization.

In a genetic screen for proteins that interact directly with Gβ (*11*), we identified Yck1, one of a pair of sister casein kinases (CKs) (*12*) that are essential for the phosphorylation of the receptor on its C-terminal cytoplasmic domain (*8*), and hence for its internalization (*7, 8*). Here we show that Gβ interacts with Yck1 on the PM and that Gβ locally inhibits receptor phosphorylation, consistent with the idea that differential phosphorylation and internalization of the receptor plays a role in the establishment of polarity. In addition, imaging and genetic data

indicate that differential receptor phosphorylation contributes to chemotropic function. A mathematical model that incorporates Gβγ inhibition of receptor phosphorylation mimics key aspects of gradient-induced receptor polarization.

RESULTS

Gβ interacts with Yck1 at the plasma membrane and is a candidate Yck substrate

To identify candidate Gβ interactors, we conducted an allele-specific dosage suppressor screen, in which we took advantage of the observation that Gβ overexpression induces the mating signal, and thereby confers cell cycle arrest (*13, 14*). A high-copy yeast cDNA library was screened for plasmids that could rescue the overexpression of wild type Gβ, but not that of an adaptive-defective mutant form of Gβ, encoded by $STE4^{A405V}$. Ten genes were identified, including Rho1 (*11*), Dse1 (*15*), and Yck1.

In addition to the Gβ-Yck1 genetic interaction, a myc-tagged form of Yck1 expressed in yeast specifically bound to a Gβγ-affinity column, as evidenced by both immunoblot and mass spec analyses (Fig. 1, A and B; Table 1). Moreover, direct physical interaction between Gβ and Yck1 in vivo was shown by bimolecular fluorescence complementation (BiFC) (Fig. 1C; Table 2). The Gβ-Yck1 BiFC signal was detectable on the PM of pheromone-treated cells prior to morphogenesis, and concentrated on the PM of mating projections in shmooing cells.

Because Gβ is phosphorylated on multiple sites in pheromone-treated cells (*16*), and because its sequence contains potential CK1 sites (*17-19*), we asked whether Gβ phosphorylation depends on Yck activity. As shown in Fig. 1D, pheromone treatment did not induce full phosphorylation of Gβ in cells lacking functional Yck1 and Yck2 (hereafter, Yck1/2). Previous genetic analyses suggested that Gβ residues T320, T322, and S335 are phosphorylated, and that full Gβ phosphorylation is dependent on the pheromone-responsive MAP kinase, Fus3 (*20*).

Mass spec analysis of Gβ phospho-peptides purified from pheromone-treated cells confirmed these phosphorylation sites and revealed one more, T318 (Figures 1E and S1). Study of mammalian CK1s suggest that they require a phosphorylated substrate and that $S/T^{P}X_{n}S/T$ (where n = 1-3) is the consensus motif (*17-19*). If this holds true for yeast, the phosphorylation of T318 or T320 would convert Gβ to a Yck1 substrate (Fig. 1E). Conversely, unphosphorylated Gβ would be expected to interact with Yck1 to a lesser degree than the partially phosphorylated species. We tested this using a mutant form of Gβ, *ste4*$^{T320A/S335A}$ (henceforth $G\beta^{P-}$), which cannot be phosphorylated (*20*). In pull-down experiments in which the relative amount of Yck1 that bound to Gβγ or $G\beta^{P-}\gamma$ beads was quantified both by immunoblot and mass spec analyses (Fig. 1, A to B; Table 1), the apparent affinity of Yck1 for $G\beta^{P-}$ was less than for Gβ. Notably, the native Yck2 (i.e., untagged and expressed at endogenous levels) was also identified by mass spec as a specific binder to the Gβγ beads, and like Yck1, showed a weaker apparent affinity for $G\beta^{P-}$ (Table 1).

Gβ overexpression inhibits phosphorylation of the receptor and promotes its polarity

Because Gβ polarizes prior to pheromone-induced morphogenesis (*21*), its direct interaction with Yck1 raises the possibility that Gβγ promotes receptor polarization by locally inhibiting receptor phosphorylation. Consistent with this, a region of hypo-phosphorylated receptor arises in response to isotropic pheromone treatment (*6, 22*). This was demonstrated using strain YDB111 (*22*), which expresses Sst2-GFP, a reporter that binds specifically to the unphosphorylated form of the receptor, and Ste2^{7XR}, a mutant form of the receptor that cannot be internalized. LatA- and pheromone-treated YDB111 cells that could not redistribute the receptor nevertheless exhibited asymmetric receptor phosphorylation (*6*).

To determine whether Gβ can inhibit receptor phosphorylation, we examined pheromone/latA-treated YDB111 cells overexpressing either Gβ, or $G\beta^{P-}$, the weaker Yck1/2-binding form of Gβ (Fig. 2, A to F). Overexpression of Gβ correlated with an increase in PM localized Sst2-GFP and greater Sst2-GFP polarity. In contrast, overexpression of $G\beta^{P-}$ did not affect the PM localization of Sst2-GFP. To further test the effect of weakening the Gβ-Yck1/2 interaction on receptor phosphorylation, we replaced *STE4* (Gβ) with *ste4*$^{T320A/S335A}$ ($G\beta^{P-}$) in strain YDB111. Pheromone and latA treatment induced significantly less PM localization of Sst2-GFP in cells expressing the native level of $G\beta^{P-}$ as compared to control cells (Fig. 2, F to G). Together, these data support the idea that Gβγ protects the receptor from Yck1/2-dependent phosphorylation, and that it does so most effectively in a discrete region of the membrane.

Local inhibition of receptor phosphorylation by Gβγ helps establish and maintain the chemotropic growth site

In time-lapse images of mating mixtures, we found that the polarized receptor crescent frequently relocalizes from the default polarity site to the chemotropic site in cells that have not yet shmooed (Fig. S2). Could asymmetric receptor phosphorylation play a role in this process? In mating mixtures of YDB111 cells, the Sst2-GFP crescent was almost always visible prior to morphogenesis and either formed initially at the eventual shmoo site, or relocated from the presumptive default site to an apparent chemotropic site prior to morphogenesis (Fig. 3). Thus, the position of minimal receptor phosphorylation anticipated the eventual site of polarized growth. Although the Sst2-GFP crescent in YDB111 cells expressing $G\beta^{P-}$ also anticipated the shmoo site, the $G\beta^{P-}$ cells shmooed about 1 time point earlier (15') than did Gβ cells ($n \geq 30$; $p = 0.05$), and did so significantly closer to the presumptive default site (Fig. 3). These data suggest two conclusions. First, cells that are unable to internalize, and thereby polarize receptor

distribution, are nevertheless able to establish a chemotropic growth site by polarizing the phosphorylation state of the receptor. Second, the role Gβ plays in positioning and stabilizing the chemotropic growth site correlates with its effect on receptor phosphorylation.

To further examine the possibility that receptor phosphorylation plays a role in chemotropism, apart from triggering receptor internalization, we replaced the native *STE2* with $STE2^{7XR}$, $STE2^{7XR\ 6SA}$, or $STE2^{7XR\ 6SD}$ in an otherwise wild type *MAT***a** strain. These alleles all encode forms of the receptor that cannot be internalized (7XR) (*23*), and which are either insignificantly phosphorylated (6SA), or which have phosphomimetic substitutions (6SD) (*24*). We then assessed the effect of the mutant receptors on chemotropism in time-lapse images of mating mixtures (Fig. 4). Cells that are fully competent to mate typically orient and shmoo directly towards their mating partner, grow chemotropically about the same distance to their point of contact, and ultimately fuse at an angle near 0˚ (Fig. 4, B[i, ii] and D). The resulting zygotes are straight and symmetrical. In contrast, cells defective in gradient sensing or chemotropism, or WT cells confused by exogenous pheromone (Fig. S3), do not orient directly toward their partners, and ultimately form angled zygotes (*21*).

When chemotropism is assayed by observing mating pairs directly rather than by quantifying the efficiency of diploid formation using genetic makers, as in McClure et al. (25), it is apparent that $STE2^{7XR}$ confers a defect in initial orientation (Fig. 4B[iii]). The mean orientation angle of the mutant cells was considerably smaller as compared to the control cells, and the mean fusion angle and the mean time to fusion were significantly greater in the WT *MAT*α X *MAT***a** $STE2^{7XR}$ mating mixtures than in the WT X WT crosses (Fig. 4, C to E). Notably, $STE2^{7XR}$ conferred an increase in mean fusion angle equivalent to the addition of exogenous pheromone to

WT mating mixtures (Fig. S3). We infer that the inability to internalize and thereby redistribute the mutant receptor compromises directional sensing.

Remarkably, when cells cannot polarize either the receptor's distribution or its phosphorylation state, they are unable to grow chemotropically. In mating mixtures, the *MAT***a** $STE2^{7XR\ 6SD}$ cells that ultimately formed zygotes with WT *MAT*α cells always polarized their growth adjacent to their last bud site. Similarly, all *MAT***a** $STE2^{7XR\ 6SA}$ cells that ultimately formed zygotes polarized their growth — or mated without undergoing morphogenesis — proximal to their last bud site. Thus, *MAT***a** $STE2^{7XR\ 6SA}$ and *MAT***a** $STE2^{7XR\ 6SD}$ cells cannot switch from the presumptive default polarity site to a chemotropic growth site, regardless of the position and proximity of potential mating partners (Fig. 4[iv-v], C).

In addition to eliminating gradient sensing in situ, the $STE2^{7XR\ 6SA}$ and $STE2^{7XR\ 6SD}$ alleles conferred pronounced defects in mating projection formation (Fig. 4F). Although most of the mating *MAT***a** $STE2^{7XR\ 6SA}$ cells and all of the mating *MAT***a** $STE2^{7XR\ 6SD}$ cells exhibited robust polarized growth, a substantial fraction of the mutants apparently could not stabilize their axis of polarity well enough to generate a tapered shmoo tip. Such cells elongate along very broad growth zones, the shape of which is easily distinguished from a normal mating projection. Of particular note, the broadly polarized *MAT***a** $STE2^{7XR\ 6SA}$ and *MAT***a** $STE2^{7XR\ 6SD}$ cells persistently turn in one direction as they elongate (Fig. 4B[v] and fig. S4), a behavior also seen in *sst2*Δ cells (*26*). Because some of these cells eventually mate, albeit over abnormally long times (Fig. 4E), their curving growth might be mistaken for chemotropism. Is the persistent turning toward the eventual fusion site a dramatic example of reorientation? Our data clearly indicate that it is not. The broadly polarized and turning *MAT***a** $STE2^{7XR\ 6SA}$ and *MAT***a** $STE2^{7XR\ 6SD}$ cells show no sign of gradient sensing. Their initial direction of growth is determined by default polarity (Fig. 4C),

and they continue to elongate and turn until they encounter a mating-competent *MAT*α cell directly in their path, often after having failed to mate with nearer potential partners (Fig. 4B[v], bottom). Only 26% of the *MAT***a** $STE2^{7XR\ 6SA}$ and *MAT***a** $STE2^{7XR\ 6SD}$ cells that elongated and turned, and 42% of those that were initially positioned within 1µm of one or more potential partners, formed zygotes within the six-hour time course (Fig. S4).

Based on our analysis of cells expressing mutant receptors in physiological gradients, we conclude that receptor internalization is required for full chemotropic function, and that receptor phosphorylation plays a critical role in chemotropism distinct from its established function as a trigger for internalization.

The pheromone receptor polarizes prior to active Cdc42

In pheromone-treated cells that are first allowed to internalize the receptor for 15 min, and then treated with latA, a polarized receptor crescent subsequently forms on the PM within about 30 min, even though ongoing actin-dependent secretion and endocytosis are blocked (*6, 27*). A likely explanation for this is that, at the time of latA treatment, a preexisting polarity site — in this case, one that is generated as the receptor is internalized — is amplified by uniform secretion together with biased docking and fusion at the membrane, as proposed by Sahin et al. (*28*). The receptor itself could be the primary determinant of this site. Although the membrane localization of the Ste2-GFP reporter falls below our detection level after 15 min of induced internalization (*6*), a concentrated receptor patch is seen when such cells are labeled with Alexa Fluor-tagged pheromone (Fig. S5). Alternatively, cortical polarity could be generated by actin-independent/Cdc42-dependent exocytosis, as described by Bendezu et al (*29*), or by endocytosis and recycling of Cdc42, as proposed by Yamamoto et al (*30*). To distinguish these possibilities,

we asked whether pheromone-induced receptor (Ste2-GFP) polarity was detectible before Cdc42-GTP (Gic2-PBD-RFP) polarity, or vice versa.

Prior to pheromone treatment, about half the cells in G1 exhibited Gic2-PBD-RFP polarity, but not Ste2-GFP polarity, whereas none showed receptor polarization alone, consistent with the essential role of Cdc42-GTP in bud emergence. Conversely, about half the G1 cells that were not yet shmooing after 60 min of pheromone treatment exhibited receptor crescents before Cdc42-GTP polarity was detectable, even though the reporter signals were of similar intensity. No pheromone-treated cells were observed that polarized Gic2-PBD-RFP before Ste2-GFP (Fig. 5, A to B).

Changes in the localization of the receptor also preceded redistribution of active Cdc42, and morphogenesis, in gradient-stimulated cells (Fig. 5, C to D). In time-lapse images of *MAT***a** cells that switched from their presumptive default polarity site to a presumptive chemotropic growth site in mating mixtures, both Ste2-GFP and Gic2-PBD-RFP moved slowly from their initial to final sites of polarization, consistent with results recently reported by Hegemann et al. (*31*). The receptor was clearly detectable and centered around the eventual polarized growth site before Gic2-PBD-RFP in 13 of 19 scored cells (68%), and was the first to fully re-localize in 13 of 16 scored cells (81%). Redistribution of Gic2-PBD-RFP was never seen to precede that of Ste2-GFP. These data strongly suggest that pheromone-induced polarity of the receptor determines the position of the chemotropic shmoo site upstream of active Cdc42.

Gβ^{P-} cells are defective in receptor polarization

Our biochemical data suggest that Gβ^{P-} has a lesser affinity for Yck1 and Yck2 than does Gβ. We have also shown that pheromone-induced polarization of GFP-Gβ^{P-} prior to morphogenesis is moderately defective (*21*). If early Gβ polarization or Gβ-Yck1 interaction play

an important role in establishing receptor polarity, then $G\beta^{P-}$ would be expected to adversely affect the formation of receptor crescents. To test this, we compared the localization of GFP-tagged receptor in Gβ and $G\beta^{P-}$ cells treated with latA 15 min after pheromone stimulation. Notably, $G\beta^{P-}$ cells exhibited reduced receptor polarization as compared to that of Gβ cells (Fig. 6, A to B), suggesting a role for Gβ phosphorylation in the establishment of the polarity site as the receptor undergoes global internalization. A similar result was observed under physiological conditions: $G\beta^{P-}$ cells exposed to pheromone gradients in mating mixtures also exhibited a defect in receptor polarization (Fig. 6, C to D).

Pheromone-induced internalization can result in the polarization of activated receptors

To follow the internalization of ligand-bound receptor distinct from the trafficking of inactive receptor, we treated cells with fluorescent pheromone. Cells were labeled on ice in medium lacking essential nutrients, and imaged at room temperature 1-2 min after being re-fed. Although the cells were not exposed to a pheromone gradient, approximately 25% exhibited an asymmetry in the rate of receptor internalization, leading to enhanced receptor polarity (Fig. S6). Thus, the surface distribution of the activated receptor can change as it internalizes. We speculate that the cell-cycle dependent polarization of the G protein (*6*) mimics the early response of cells to gradient-stimulation, revealing the possibility of polarization via differential internalization.

$G\beta^{P}\gamma$-Yck interaction is critical in a reaction-diffusion model that mimics gradient-induced receptor polarization upstream of directed secretion

The observations presented here suggest a novel mechanism for the establishment of pheromone-induced receptor polarity. By interacting with Yck1/2, Gβγ inhibits receptor phosphorylation, which in turn, slows receptor internalization. The Gβγ-Yck1/2 interaction is also expected to inhibit endocytosis of the G protein, as we have found that both Gα and Gβγ

internalize with the receptor (*6*). Initially, a shallow gradient of pheromone is mirrored by a similarly shallow gradient of occupied receptor across the cell. This slight differential in activated receptor should lead to a corresponding differential of free Gβγ. As receptor and G protein in this area are less likely to be internalized, a positive feedback loop is created which, in combination with other mechanisms, rapidly amplifies the intracellular signaling gradient prior to the nucleation of actin cables (Fig. 7A).

Previously published data suggest that Gα recruits the activated Fus3 MAPK to phosphorylate cortical Gβ *(32, 33)* and demonstrate roles for the Gα-Fus3 interaction in directional sensing and chemotropic shmooing (*21, 33, 34*). Given the data reported here, MAPK phosphorylation of Gβ would be expected to enhance its interaction with Yck1/2. This raises the possibility that two positive feedback loops — (1) Gα/Fus3 mediated phosphorylation of Gβ and (2) inhibition of Yck-dependent internalization of the receptor and G protein by phosphorylated Gβ — act synergistically to promote receptor polarization.

To determine whether our postulated feedback mechanisms can explain how receptor polarity is generated in response to a pheromone gradient, we developed a reaction/diffusion model which, unlike other mathematical models of yeast chemotropism (*35-37*), is based on mechanisms that are independent of Cdc42 (Fig. 7, B to D, Fig. S7, and Tables S3-S6). We first created a core network that includes only the best-characterized components. Network 1 comprises the receptor-pheromone interaction, G protein cycle, and Yck-dependent internalization of the receptor and G protein. Network 2 adds the $G\beta^{P}\gamma$-Yck interaction and Network 3 adds the Gα-Fus3 interaction. As shown in Fig. 7E, a 10 → 5 nM pheromone gradient induces a drastic reduction in the number of receptors on the PM of a computational yeast cell lacking downstream regulation of receptor internalization, with no resulting polarity

(Network 1). In contrast, a computational cell that differs only in the addition of the $G\beta^{P}\gamma$-Yck interaction (Network 2; Fig. 7F) responds to the same gradient by robustly polarizing its receptor. Addition of the Gα-Fus3 feedback loop (Network 3; Fig. 7G) results in faster polarization. Notably, the rate of receptor internalization is highest on the up-gradient side of the cell immediately after pheromone stimulation, as expected due to higher receptor occupancy in this area (Fig. S8). Within 12 min (Network 3), or 15 min (Network 2), however, iteration of the feedback loops reverses the differential so that receptor internalization is slowest at the front of the cell, where the receptor eventually polarizes.

Output from the mathematical model also yielded interesting and testable predictions about the spatio-temporal dynamics of other key signaling elements in the response networks. Whereas the heterotrimeric G protein remains largely uniform on the surface of the gradient-stimulated computational cell, activated Gα and free Gβγ polarize along with the receptor (Fig. S9). At the same time, inverse intracellular gradients of free Yck (back) and Gβγ-bound Yck (front) are generated (Fig. S10).

DISCUSSION

Although both chemotactic and chemotropic cells employ GPCRs to detect and respond to chemical gradients, they differ in how they deploy their surface receptors. With few exceptions, chemotactic cells exhibit a uniform surface distribution of receptors. This enables them to rapidly sense changes in ligand concentration in three dimensions. Although the surface distribution of receptors is uniform, the distribution of activated receptor reflects changes in the gradient within seconds. Local receptor activation is amplified by downstream signaling mechanisms, leading to polarized cellular outputs (*38, 39*). By comparison, chemotropism is a slower and more nearly two-dimensional process. As exemplified by budding yeast, chemotropic

growth occurs on a timescale of tens of min rather than seconds, and on solid surfaces rather than in fluid or tissues. These spatiotemporal differences may underlie the redistribution of receptor to the region of polarized growth in pheromone-stimulated cells, as compared to the invariant receptor display on the surface of chemotactic cells.

The formation of polarized receptor crescents in shmooing yeast was first reported in 1991 (*40*), and its significance has been debated ever since. Is receptor polarization simply the result of global internalization followed by actin-cable directed secretion, or does the local concentration of receptor determine the position of the chemotropic growth site? A number of results indicate that the initial polarization of surface receptor is established independently of actin-cable directed secretion. Polarized receptor crescents are easily visualized before morphogenesis (*6*, *31*) and before the alignment of actin cables towards the growth site (Stone and Sukumar, unpublished observation). Pheromone-treated cells in which actin-cable directed secretion has been disabled by mutation or drug nevertheless form robust receptor crescents (*6*, *31*). Here, we report that receptor crescents form before the polarization of active Cdc42 in pheromone-treated G1 cells (Fig. 5), implying that the receptor polarizes upstream of actin-cable nucleation.

In contrast to the robust receptor polarization we observe in the absence of directed secretion, the receptor cannot polarize if its internalization is blocked by mutation or by treatment with latA concomitant with pheromone (*6*). However, if pheromone-induced receptor internalization is allowed to continue for 15 min before actin is depolymerized with latA, robust receptor crescents subsequently appear (*6*; Fig. 6). We infer that a polarity site is established while the receptor is being internalized, and that its position is most likely determined by the receptor itself. A mutant form of the receptor that cannot be internalized, and is thus unable to

polarize ($Ste2^{7XR}$), confers a defect in gradient sensing, as measured in low-density unilateral mating mixtures (Fig. 4). Moreover, the receptor crescent can be seen to shift from the default polarity site to the chemotropic growth site in WT cells that have not yet changed shape (Fig. S2). Taken as a whole, these data indicate that receptor polarization occurs upstream of directed secretion and contributes to gradient sensing.

In addition to suggesting that the distribution of the receptor and G protein can be polarized by differential internalization, our data indicate that polarizing the phosphorylation state of the receptor alone can support a chemotropic response. In mating cells that cannot internalize the receptor, the unphosphorylated receptor crescent was often seen to move from the presumptive default polarity site to an apparent chemotropic site in advance of morphogenesis — i.e., the unphosphorylated receptor crescent responded to the gradient and anticipated the eventual shmoo site (Fig. 3). Because the distribution of unphosphorylated receptor cannot be determined using the Sst2-GFP reporter in wild type cells, we measured the effects of preventing receptor internalization and phosphorylation on chemotropism in otherwise wild type cells stimulated by natural gradients. In contrast to the moderate orientation defect seen in $Ste2^{7XR}$ cells, $Ste2^{7XR\ 6SA}$ and $Ste2^{7XR\ 6SD}$ cells that can neither internalize nor phosphorylate their receptor were unable to switch from default to chemotropic polarity, and were severely compromised in their ability to form mating projections (Fig. 4 and fig. S4). These data indicate that receptor phosphorylation plays an essential role in chemotropism distinct from its role as a trigger for receptor internalization, and suggest that localized concentration of unphosphorylated receptor (i.e., polarization of the receptor's phospho-state) is critical to establishing the chemotropic growth site.

The processes that enable yeast cells to align their mating projection sites with pheromone gradients are not well understood. However, two relevant mechanisms have been identified. The binding of free Gβγ to Far1-Cdc24-Bem1 was established early in the study of yeast chemotropism (*4, 5*). It was subsequently shown that disrupting either the Gβγ-Far1 interaction (*4*) or the Gβγ-Cdc24 interaction (*5*) prevents chemotropic shmooing. More recently, Dyer et al. (*35*) and Hegemann et al. (*31*) used live-cell imaging to show that a dynamic polarity complex — likely composed of the core constituents Bem1, Cdc24, Cdc42, and Bni1 — moves in a random walk around the cortex of vegetative cells. When cells are exposed to pheromone, the movement of the polarity complex is biased toward the incipient shmoo site via the interaction of Far1-Bem1-Cdc24 with free Gβγ (*27*, *34*). In principle, therefore, yeast chemotropism can be explained as follows: A gradient of pheromone induces a gradient of activated receptor on the surface of the cell, which in turn, is mirrored by a gradient of activated G protein. Free Gβγ then restricts the movement of the polarity patch along the cell cortex on the up-gradient side of the cell, and ultimately stabilizes it position at the incipient growth site. Actin cables are subsequently nucleated at this site.

As the primary determinant of the chemotropic growth site downstream of the receptor, Gβγ must be locally concentrated or otherwise differentiated (e.g., by phosphorylation) where the pheromone concentration is highest. Its polarization is required to constrain the polarity patch and nucleate actin cables. There are two challenges to explaining how Gβγ polarizes before polarity patch stabilization and actin-cable nucleation. First, physiological gradients are shallow. It has been estimated that a 1% difference in receptor occupancy across the 5μm length of a yeast cell in a pheromone gradient is sufficient to elicit robust orientation toward the pheromone source (*42*), and microfluidic studies suggest an even greater acuity (*36*). This means that

although there is a slight excess of free Gβγ on the up-gradient side of the cell, there is almost as much on the down-gradient side. Second, because activated receptors are targeted for phosphorylation and internalization, the density of receptor and G protein on the PM is expected to be lowest where the pheromone concentration is highest —the opposite of what would be expected to drive chemotropism.

The Gβγ-Yck interaction we demonstrate here (Fig. 1, A to C; Tables 1-2) provides a means to invert the relationship between receptor activation and receptor internalization. From first principles, the proportion of activated receptors on the surface of a cell subjected to a pheromone gradient should increase as a function of pheromone concentration. Based on the established model of pheromone-induced receptor modification and endocytosis, the initial rate of receptor internalization is expected to be greatest where the density of activated and phosphorylated receptors is greatest. So too is the initial rate of heterotrimeric G protein activation. We postulate that free Gβγ protects proximal receptors from Yck-dependent phosphorylation and internalization, which in turn, preserves heterotrimeric G proteins on the PM (*6*). Thus, the slightly greater burst of Gβγ released from Gα on the up-gradient side of the cell triggers a feedback loop that amplifies signaling at the incipient shmoo site. As yet, the most upstream event in this pathway is the induction of phospho-receptor polarity such that the most concentrated region of activated-unphosphorylated receptor marks the direction of the gradient source.

Based on published results and observations presented here, we also postulate a feedback loop that promotes the Gβγ-Yck interaction. Activated Gα is thought to recruit active Fus3 to the cell cortex (*32, 33, 43*), where it phosphorylates Gβ (*20*) on one or more MAPK consensus sites (see Fig. 1E). Given the CK1 consensus motifs in the Gβ sequence (*17-19*), MAPK

phosphorylation of either T318 or T320 could convert Gβ to a Yck substrate. Indeed, Gβ is hypo-phosphorylated in cells lacking Yck1/2 function (Fig. 1D). These various points can be unified as follows: Yck has a basal affinity for unphosphorylated Gβ, which is increased when Gβ is phosphorylated by Gα-recruited Fus3. Thereby marked as a Yck substrate, Gβ acts as a competitive inhibitor of receptor phosphorylation. Alternatively, Gβ might allosterically downregulate Yck catalytic activity. Although it will be of interest to distinguish these possibilities, Gβ protection of proximal receptors could involve either or both mechanisms.

We conclude that, like the chemotactic cells, yeast cells unable to polarize the distribution of receptor can nevertheless orient in a gradient, albeit not as well as wild type cells. How do they do this? A likely explanation is that as they polarize the phosphorylation state of the receptor, G protein activation is favored where the active-unphosphorylated receptor is concentrated. This requires that the G protein be able to freely diffuse on the PM and be subject to activation by coupling with liganded-receptors, as has been reported for chemotactic cells. In *Dictyostelium*, for example, activated Gα and free Gβγ are thought to be concentrated on the leading edge of chemotaxing ameba when freely diffusing heterotrimeric G proteins couple with liganded receptors on the up-gradient side of the cell (*44, 45*). The output from our mathematical model is consistent with this hypothesis: Although the heterotrimeric G protein is almost uniformly distributed on the surface of the gradient-stimulated computational cell, activated Gα and free Gβγ dramatically polarize along with the active receptor (Fig. S7 and S8). It remains to be determined whether the liganded-unphosphorylated receptor activates the G protein more effectively than the liganded-phosphorylated receptor, and if so, how it does so. If confirmed, however, a confined G-protein activation center would add another powerful feedback mechanism to our proposed networks. In this scenario, activated receptor would generate

activated Gα and free Gβγ, which would increase the local density of activate/unphosphorylated receptor and G protein, which would further increase the local density of activated Gα and free Gβγ, and so on. As discussed above, the rapid localization of Gβγ toward source of the gradient is essential for positioning the chemotropic growth site.

Together, our data suggest that polarity is first established in response to a pheromone gradient by differential phosphorylation and internalization of the receptor, which depends in turn, on asymmetric protection of the receptor by its G protein. At least two inter-connected positive feedback loops are at the heart of the localized amplification mechanism underlying the yeast chemotropic response. Similar processes may contribute to directional sensing in other systems, as a role for GPCR phosphorylation other than desensitization has been reported in *Dictyostelium* chemotaxis (*46*).

MATERIALS AND METHODS

Molecular and microbiological techniques. Standard methods were used for microbial culture and molecular manipulation (*47-49*).

Yeast strain construction. The yeast strains used in this study are listed in Table S1. Unless noted otherwise, they were derived by transformation from strain 15Dau (*MAT***a** *bar1*Δ *ade1 his2 leu2-3*, *-112 trp1 ura3*Δ), which is congenic with strain BF264-15D (*50*). To create strains that can be heavy-labeled for mass spec analysis, *ARG5,6* was knocked out in strains 15Dau and RDY114 by transplacement with a fragment containing KanMX4 G418, PCR-amplified from pFA6-kanMX4 (*51*), flanked by ends homologous to *ARG5,6*, using the oligomers:
5'-TCCAAATTCCAAAAATTTG
TGTCTTCATTAAACAAATCCACCATAGCAGGCGTACGCTGCAGGTCGAC-3' and

5'-TCAGGGATACCAGCATACTCTCCATAACCCATAGCAAGATTAATATTTTGATCGA TGAATTCGAGCTCG-3'. Integrants were selected on medium containing 200 mg/L Geneticin G418. *LYS1* was then transplaced with a TEF promoter-hph-TEF terminator fragment amplified from the pAG32 plasmid (EUROSCARF) and flanked by ends homologous to *LYS1* using the oligomers: 5'-GCTGCCGTCACATTAC ATCTAAGAGCTGAAACTAAACCCCTAGAGGCTCTGTTTAGCTTGCCTTGTC-3' and 5'-GTACCAGAACGGTAGGTTTGTTAAACACAGTAGCCACAGTGTATATGCTC GTTTTCGACACTGGAT-3'. Integrants were selected on medium containing Hygromycin B. To allow for exclusive expression of 6xHis-Ste18, and 3xHA-Ste18, native *STE18* (Gγ) was transplaced with a fragment containing *URA3* as described previously (*52*). Strain AIY109 was created by integrating $ste4^{T320A\ S335A}$ into strain YDB111 (*22*) in situ, using Msc1-cut YIplac128/$ste4^{T320A\ S335A\ N\Delta112}$ (pAIB130). Strain AIY197 was created by integrating Hpa1-cut LHP1921 (*53*) into RDY114 (*21*). Strain AIY301 was created by integrating Apa1-cut YIplac211-GIC2-PBD-RFP (*54*) into DMY169 (*6*). Strains XWY005, XWY008, and XWY018 were created by integrating Cla1-cut DLB3850, DLB3784, and DLB3851, respectively, into strain DSY257. The fluorescent marked *MAT*α mating tester strain, XWY027, was generated by integrating Bsu361-cut pRS406/GFP-BUD1 at the *BUD1* locus of DSY129. All integrations intended to create gene deletion, replacement, or in-situ tagging were checked by genomic sequencing.

Plasmid construction. The plasmids used in this study are listed in Table S2. YCplac22/GAL1-3xHA-STE18 was constructed by PCR-amplifying *STE18* from pGEX-KG-STE18 (MCB35) with the oligomers: 5'-TGCTATCCAGTCGACATGTACCCATACGA

CGTCCCAGACTACGCTTACCCATACGACGTCCCAGACTACGCTTACCCATACGACGT
CCCAGACTACGCTATGACATCAGTTCAAAACTC-3', in which the underlined sequence encodes the N-terminal 3X-HA tag, and
5'-TGGACCGCCAAGCTTTTACATAAGCGTACAACAAA-3'. The SalI-HindIII cut PCR product was inserted into YCplac22/*GAL1* (*55*). YIplac128/ste4$^{T320A\ S335A\ N\Delta112}$ was constructed by PCR-amplifying *ste4*$^{T320A\ S335A}$, minus the first 112 bases of the coding region, from RDY120 (*21*) using the oligomers 5'-CGCGAATTCTGCGCTTCCACAGAACTAATG-3' and 5'-CGCGGATCCAAATAGAGGCCGCCAGACAAG-3'. The PCR fragment cut with EcoRI and BamHI was subcloned into YIplac128 (*55*) to create AIB130. pRS415/ADH1-STE4-VF2 was constructed by PCR-amplifying genomic *STE4* lacking the stop codon using the oligomers 5'-GCAGGATCCGATGGCAGCACATCAGATGG-3' and 5'-GCTGGATCCTTGATAACCTGGAGACCAT-3'. The BamHI-cut PCR fragment was subcloned into p415-VF2 (*56*) in frame with the C-terminal Split-Venus fragment under the control of the *ADH1* promoter to create AIB201.

Gβ-Yck1 Split-Venus bimolecular fluorescence complementation (BiFC) assay. Because constitutive overexpression of Gβ causes permanent cell cycle arrest, the Gβ-Yck1 BiFC assay was performed in a strain that allows conditional expression of *STE7*. *MAT***a** *STE7*Δ*::KanMX* YCplac22/GAL1-STE7 cells transformed with pRS416/ADH1-VF1-YCK1 and pRS415/ADH1-STE4-VF2 (AIY273), pRS416/ADH1-VF1-YCK1 and pRS415/ADH1-VF2 (AIY276), or pRS415/ADH1-STE4-VF2 and pRS416/ADH1-VF1 (AIY275) were grown to mid-log phase in selective medium containing 2% sucrose and induced with 2% galactose for 1 hr before being treated with 150nM α-factor. Images were acquired 2.5 hrs after pheromone treatment using an ANDOR Revolution XD spinning disk laser confocal system with a motorized Olympus IX-81

microscope, a Yokogawa CSU-X1 spinning disk unit, motorized XYZ control (piezo), and an iXon897 EMCCD camera controlled by Andor iQ2 software. A UplanSApo NA 1.4x100 objective was used with a laser excitation of 488 nm. The mean PM and mean cytoplasmic fluorescence were quantified using the ImageJ segmented line tool and selection brush tool, respectively.

Gβ phosphorylation assay. DMY222 (*MAT***a** *his3 leu2 ura3-52 yck1-D1::ura3 yck2-2^{ts} leu2*:*STE2-GFP::LEU2*) and the congenic strain DMY224 (*MAT***a** *his3 leu2 ura3-52 leu2*:*STE2-GFP::LEU2*) were grown to mid-log phase at room temperature (RT) in rich medium (YEPD), shifted to 37˚C (restrictive temperature) or maintained at RT, and treated with either 150 nM α-factor or 1.2 μM α-factor for 1 hr. Cell equivalents were collected from all cultures and the phosphorylation state of Gβ was assayed by immunoblotting as described (*20*), using affinity-purified antisera raised against full-length Gβ (*57*).

Gβ and Gβ^{P-} overexpression assay. Strains XWY011 (Ga11-Gβ), XWY033 (Gal1-Gβ^{P-}), and RDY102 (GβΔ) were grown to mid-log phase at 30˚C in selective medium containing 2% sucrose, and galactose was added to a final concentration of 2%. Cell equivalents were collected after 0 and 2 hr of induction, and protein concentration in the cell lysates was determined by Bradford assay. 30 μg total protein per sample was run on a 4-20% gradient gel (Bio-Rad, Hercules, CA), and the amount of Gβ was assayed by immunoblotting as described above.

Gβγ/Gβ^{P-}γ affinity beads and pull-down analysis. To prepare Gβγ-affinity and negative control beads, strains NWY069, NWY068, and NWY071 were grown to mid-log phase in selective medium containing 2% sucrose and 0.1% dextrose, induced with 2% galactose for 5 hr, then treated with 150 nM α-factor for 1 hr. Cells were harvested at 2300 x *g* at RT, washed once with ice-cold deionized water, and frozen in dry-ice ethanol. Cell pellets were lysed at 4˚C with

0.5 mm silica beads in 1X TBS buffer containing protease inhibitors (150 mM NaCl, 10 mM Tris pH 8, 100 mM PMSF, 2 mM aprotinin, 2 mM pepstatin, 2 mM leupeptin). Crude lysates were centrifuged at 16100 x *g* at 4˚C for 20 min and protein concentrations were determined using the Pierce 660nm assay kit from ThermoFisher (Rockford, IL). 7.3 mg of each lysate was mixed with 30 µL ThermoFisher anti-HA agarose beads, adjusted to 1.25 ml total volume with 1X TBS buffer containing protease inhibitors, and incubated for 2 hr at 4˚C with end-over-end rotation. The beads were washed 3 times with 1X TBS-T buffer (150 mM NaCl, 10 mM Tris pH 8, Tween-20 0.1%). To obtain lysate containing myc-Yck1, strain NWY073 was cultured and processed as above except that it was galactose-induced for 3 hrs. Low and high amounts of total protein from the NWY073 lysate, 225 µg (L) and 900 µg (H), were added to the Gβγ/Gβ^{P-}γ-affinity beads. Volumes were adjusted to 1.25 ml with 1X TBS buffer containing protease inhibitors and the slurries were incubated at 4˚C for 1 hr with end-over-end rotation. The beads were washed 3 times with 1X TBS-T buffer, and then reduced in 1X SDS sample buffer. The supernatant was split into two fractions for immunoblot and mass spec analysis. In the immunoblot analysis, myc-Yck1 was detected using mouse anti-c-myc HRP conjugated antibody (1:900) from ThermoFisher; 3x-HA-Gγ was detected using primary mouse anti-HA antibody (1:900) from Covance (Princeton, NJ) and secondary goat anti-mouse IgG_1 HRP conjugated antibody (1:400,000) from Jackson ImmunoResearch Inc. (West Grove, PA). Densitometric analysis of scanned immunoblot films was performed with the ImageJ gel analysis tool, which provided absolute intensity values (AI) of each band. The relative amount of myc-Yck1 binding to Gβγ vs. Gβ^{P-}γ was determined by subtracting the corresponding negative control signal (L or H), and then taking the ratio of the resulting signal-above-noise values. Normalization to HA-Gγ was not necessary, as the αHA signal did not vary from lane to lane. For the mass spec analysis,

225 μg of total protein from the NWY073 lysate was incubated with the affinity beads. Eluted proteins were alkylated, and separated by PAGE. The ~70-55 kDa (myc-Yck1 and Yck2) and 55-45 kDa (myc-Yck1 cleavage products; Gβ) regions of the gel were then excised, the proteins in-gel digested with sequencing-grade modified trypsin from Promega (Madison, WI), and the resulting trypsin fragments analyzed by nanoscale LC-MS/MS, as previously described (*58, 59*).

Phospho-peptide analysis of Gβ. NWY052 cells were grown to mid-log phase in selective synthetic 2% sucrose medium containing natural arginine and lysine (normal Arg/Lys), and induced with 2% galactose for 5.5 hrs (light culture). A parallel culture of NWY052 was SILAC labeled in medium containing 20mg/L heavy Arg/Lys (L-lysine:2HCL, U-13C6 and L-Arginine: HCL U13C6, U-15N2) (Cambridge Isotope Labs, Tewksbury, MA), and treated with 150 nM α-factor for 1 hr after galactose induction. The light and heavy cultures were prepared for mass spec analysis in parallel. Cells were harvested at 2300 x *g* at RT, washed once with ice-cold deionized water, and frozen in dry-ice ethanol. Cell pellets were lysed at 4˚C with 0.5 mm silica beads in 1X TBS buffer containing protease and phosphatase inhibitors (150 mM NaCl, 10 mM Tris pH 8, 100 mM PMSF, 2 mM aprotinin, 2 mM pepstatin, 2 mM leupeptin, 1 mM sodium orthovanadate, 50 mM NaF, 10 mM sodium pyrophosphate, 10 mM β-glycerol phosphate). Crude lysates were centrifuged at 16100 x *g* at 4˚C for 20 min and protein concentrations were determined using the Pierce 660nm assay kit. 25mg of total protein from each lysate was mixed with 100 μL Ni-NTA beads from Qiagen (Hilden, Germany). Volumes were adjusted to 1.25 ml with 1X TBS buffer, containing protease and phosphatase inhibitors, and the slurries were incubated at 4˚C with end-over-end rotation for 16 hr. The beads were washed 10 times with 1X TBS-T buffer (150 mM NaCl, 10 mM Tris pH 8, Tween-20 0.1%), and then reduced in 1X SDS sample buffer. Equal volumes of supernatant from heavy and light cultures were mixed. The

proteins were alkylated and separated by PAGE. The ~50-45 kDa region of the gel was excised and subjected to in-gel digestion with sequencing grade modified trypsin from Promega (Madison, WI). Peptides were vacuum concentrated and enriched for phospho-peptides by use of a TiO_2 phosphopeptide enrichment and clean-up kit from Pierce biotechnology (Rockford, IL). Phospho-peptides were vacuum concentrated and analyzed by nanoscale LC-MS/MS as previously described (*58-60*).

Sst2-GFP, Ste2^{7XR}-mCherry, and Ste2-GFP localization in G1-synchronized cells. G1-synchronized cells were purified by elutriation as previously described (*6*). Cells used to study the localization of Sst2-GFP and Ste2^{7XR}-mCherry (strains AIY100, AIY101, and AIY221) were spun down and resuspended in selective synthetic medium containing 2% galactose, cultured for 1 hr at 30°C, then treated with 1.2 μM α-factor and 200 μM of lactrunculin A (LatA). Cells used to study the localization of Ste2-GFP (strains DMY169 and AIY197) were spun down and resuspended in synthetic medium containing 1.5% sucrose and 0.5% dextrose, treated with 9 nM α-factor at 0', and with 200 μm LatA 15 min later. All cultures were maintained at 30°C. Images were acquired at 15-minute intervals using an Axioskop 2 microscope (Carl Zeiss, Jena, Germany) with a 100x oil immersion objective and a digital AxioCam camera. Laser excitation was 488 nm. Images were processed with Zeiss AxioVision software (Carl Zeiss).

Time-lapse Sst2-GFP and Ste2-GFP localization in mating mixtures. Wild type *MAT*α cells and experimental *MAT***a** cells were grown to mid-log phase in synthetic 2% dextrose medium, mixed 1:1, and spread at a density of A_{600} = 1.0 on agarose pads made from synthetic dextrose medium. Mating mixtures were maintained at 30°C using an Okolab chamber. DIC and fluorescent (488-nm excitation) images were acquired from 6 fields at 15 min intervals using the spinning disk microscope described above. To follow the localization of Sst2-GFP, 21 z-sections

were acquired over 6 μm. Images were sum-projected using ImageJ and the orientation and reorientation angles were quantified as described in the Fig. 2 legend. To follow the localization of Ste2-GFP, fifteen z-sections were acquired over 4.2 μm. Images were sum-projected using ImageJ and the signal intensity along the insipient long axis of the cell was quantified using BudPolarity (*61*).

Time-lapse zygote formation in mating mixtures. GFP-Bud1 labeled *MAT*α cells (XWY028) and experimental *MAT***a** cells were grown to mid-log phase in synthetic 2% dextrose medium, mixed 1:1, and spread at a density of 14,000 cells/mm^2 on agarose pads made from synthetic dextrose medium. Mating mixtures were maintained at 30°C using a DeltaVision environment control chamber (GE Healthcare Bio-Sciences, Pittsburgh, PA, USA). Images were acquired from 20 fields at 15-minute intervals using a DeltaVision Elite microscope (GE Healthcare Bio-Sciences) with a 60x oil immersion objective and a Front Illuminated sCMOS digital camera. To follow details of cell growth and zygote formation, DIC images were acquired in 31 z-sections over 6 μm. To identify the *MAT*α cells, fluorescent images (461-489 nm excitation) were acquired at the center slice. Images were processed with ImageJ software. Initial orientation angles, fusion angles, time of fusion, and morphologies of *MAT***a** cells were quantified and analyzed as described in the Fig. 4 legend.

Ste2-GFP and Gic2-PBD-RFP localization in asynchronous cells. AIY301 cells were grown to mid-log phase at 30°C in selective medium containing 2% sucrose, and treated with 15 nM α-factor. Images were acquired 1 and 2 hours later using an Axioskop 2 microscope as described above. RFP and GFP were visualized using laser excitations of 561 nm and 488 nm, respectively. Exposures and processing were identical for all images.

Time-lapse Ste2-GFP and Gic2-PBD-RFP localization in mating mixtures. Wild type *MAT*α (DSY129) cells and experimental *MAT***a** cells (AIY301) were grown to mid-log phase in synthetic 2% dextrose medium, mixed 1:1, and spread at a density of 14,000 cells/mm^2 on agarose pads made from synthetic dextrose medium. Mating mixtures were maintained at 30°C using a DeltaVision environment control chamber. Images were acquired from 15 fields at 7.5-minute intervals using a DeltaVision Elite microscope with a 60x oil immersion objective and a Front Illuminated sCMOS camera. To follow the localization of the Ste2-GFP and Gic2-PBD-RFP reporters, fluorescent images were acquired in 3 z-sections over 1 μm using LED excitations of 461-489 nm and 529-556 nm, respectively. Images were processed with ImageJ software. Polarity establishment (PE), polarity switch (PS), and polarity fixed (PF) were determined as described in the Fig. 5 legend.

Receptor labeling and internalization assays. The surface-expressed α-factor receptor, Ste2, was labeled with Alexa Fluor 594-conjugated α-factor according to the method of Toshima et al. (*62*). To determine how the density and distribution of the receptor changes over time in response to pheromone, DMY169 cells were G1-synchronized by elutriation and treated with 6 nM α-factor at 30°C in YEPD. Aliquots were taken at 5 min intervals, treated with 10 mM sodium azide, and incubated with the labeled α-factor (a generous gift from Dr. David King). The *MAT***a** *ste2*Δ strain (EDY208) was used as a negative control for receptor labeling. Images were acquired using an ANDOR Revolution WD spinning disk laser confocal system with a motorized Olympus IX-81 microscope, a Yokogawa CSU-W1 spinning disk unit, a Prior motorized stage, and a neo sCMOS camera controlled by Andor iQ2 software. A UPLSAPO 60x Silicon immersion objective (NA 1.3) was used and 9 z-sections were acquired over 4.8 μm using a laser excitation of 561-nm; one center slice was imaged with DIC. Images were sum-

projected using ImageJ. To assay the relative rate of receptor internalization as a function of position on the PM, *MAT***a** cells (RDY126) were grown to mid-log phase in YEPD medium, labeled with Alexa Fluor 594-conjugated α-factor, and imaged at 1-minute intervals at RT using the system described above. Nine z-sections were acquired over 5.6 µm using a laser excitation of 561-nm and 1 center slice was imaged with DIC. Images were sum-projected and membrane fluorescence was obtained using the segmented line tool of ImageJ.

Relative rates of labeled-receptor PM signal decay. High frequency PM noise was filtered out of the live-cell imaging data using a moving average function with the sliding window equal to $1/10^{th}$ of the membrane perimeter. For the position x at time t in cell c with a window size w, the fluorescence intensity was calculated by the following formula:

$$\mathrm{FI_n}(x,t,c) = \mathrm{avg}\left[\mathrm{FI_o}(x-\tfrac{w}{2},t,c),\ldots,\mathrm{FI_o}(x+\tfrac{w}{2},t,c)\right],$$

where $\mathrm{FI_n}$ denotes the new value after filtering, and $\mathrm{FI_o}$ the original raw value. Background was removed by subtracting the minimum value from each data set

$$\mathrm{FI}(x,t,c) = \mathrm{FI_n}(x,t,c) - \min_{x,t} \mathrm{FI}_n(x,t,c).$$

Assuming the kinetics of internalization resemble a 1st order chemical reaction, we calculated the relative fluorescence intensity of time point t compared to time point 0 to determine how membrane receptor density changes with time using the following formula:

$$\mathrm{FI}_r(x,t,c) = \mathrm{FI}(x,t,c)/\mathrm{FI}(x,0,c)$$

Finally, we used the data set for each cell to ask whether a discrete region of the PM exhibited a significantly slower rate of signal loss than the remainder of the PM. This was determined by fitting the 10 values for each pixel (time points 0-9) to the exponential decay formula:

$$\mathrm{FI}(x,t,c) = A\ exp(-\lambda t)$$

where the decay rate λ and initial quantity A are two parameters to be fitted. A putative area of receptor protection was defined as the points that were in the 30th percentile for decay rate (i.e., the slowest 30%). We calculated the average FI_r of the "protected region" and compared it to the average of the rest of the cell. In some cases the protected region was fragmented. The regions were connected if the distance between them was less than 1/10 of the perimeter of the cell and the average decay rate of region after connecting was still above the threshold.

Computational model of pheromone-induced receptor polarization

Spatial model of yeast cell

To model the plasma membrane of a yeast cell, we used a sphere, the surface of which was partitioned into patches by *n* latitude and *m* longitude lines, uniformly spaced (Fig. S7). The center of each patch was used to represent its position. The surface distances between neighboring patches are given by equations (Eq.) 1 & 2 (Table S3). The *j*-th patch in the *i*-th band can be denoted by an index pair (*i,j*). The position of the (*i,j*) patch, (x_{ij}, y_{ij}, z_{ij}), is given by Eq.3. In each patch, we stimulated the reaction network model with the pheromone concentration appropriate to its position. Because the pheromone gradient is aligned along the *x*-axis, and the pheromone concentration is assumed to change linearly with *x*, only x_{ij} is needed to determine the local pheromone concentration of the (*i,j*) patch (Eq.4). All proteins were assumed to diffuse laterally, as only the PM was modeled in this analysis. If the effect of surface curvature is ignored, the diffusion of each molecular species can be obtained from equations 5-7 (Table S3).

Networks

To model pheromone-induced receptor polarization upstream of directed secretion, and to evaluate how our postulated feedback mechanisms affect the establishment of receptor polarity, we first created a core network that includes only the most basic and best characterized

components. Network 1 comprises the receptor-pheromone interaction, G protein cycle, and Yck-dependent internalization of the receptor and G protein (Fig. 4B). Network 2 adds the $G\beta^{P}\gamma$-Yck interaction (Fig. 4C) and Network 3 adds the Gα-Fus3 interaction (Fig. 4D). The mathematical representation of these networks is detailed in Tables S4-S6. A common set of coupled partial differential equations (PDEs) was derived from their corresponding reaction formulae. Each PDE describes how the concentration of a given molecule changes over time and space. Differences in the topology of the three networks were accounted for by varying the initial values of the relevant parameters (color-coded in Table S4).

SUPPLEMENTARY MATERIALS

Figures S1-S7

Fig. S1. Examples of mass spectra used to map the sites of pheromone-induced Gβ phosphorylation.
Fig. S2. Dynamic localization of the pheromone receptor as cells orient toward mating partners.
Fig. S3. Exogenous pheromone induces formation of angled zygotes
Fig. S4. Time-lapse images of elongating and turning *MAT***a** $STE2^{7XR\ 6SA}$ and *MAT***a** $STE2^{7XR\ 6SD}$ cells in mating mixtures
Fig. S5. Surface distribution of receptor assayed by Alexa Fluor 594-conjugated α-factor binding.
Fig. S6. Receptor internalization assay
Fig. S7. Spatial model of the computational yeast cell.
Fig. S8. Computational model of receptor dynamics.
Fig. S9. Computational model of G protein dynamics.
Fig. S10. Computational model of Yck dynamics.

Tables S1-S6

Table S1. Yeast strains used in this study
Table S2. Plasmids used in this study
Table S3. Equations used for the spatial model of the yeast cell
Table S4. Definitions and parameters
Table S5. Reaction formulae
Table S6. Partial differential equations
References (63-68)

REFERENCES

1. L. Bardwell, A walk-through of the yeast mating pheromone response pathway. *Peptides* **26**, 339-350 (2005).
2. D. Pruyne, A. Bretscher, Polarization of cell growth in yeast. I. Establishment and maintenance of polarity states. *J Cell Sci* **113 (Pt 3)**, 365-375 (2000).
3. D. Pruyne, A. Bretscher, Polarization of cell growth in yeast. *J Cell Sci* **113 (Pt 4)**, 571-585 (2000).
4. A. C. Butty, P. M. Pryciak, L. S. Huang, I. Herskowitz, M. Peter, The role of Far1p in linking the heterotrimeric G protein to polarity establishment proteins during yeast mating. *Science* **282**, 1511-1516 (1998).
5. A. Nern, R. A. Arkowitz, A Cdc24p-Far1p-Gβγ protein complex required for yeast orientation during mating. *J Cell Biol* **144**, 1187-1202 (1999).
6. D. V. Suchkov, R. DeFlorio, E. Draper, A. Ismael, M. Sukumar, R. Arkowitz, D. E. Stone, Polarization of the yeast pheromone receptor requires its internalization but not actin-dependent secretion. *Mol Biol Cell* **21**, 1737-1752 (2010).
7. L. Hicke, H. Riezman, Ubiquitination of a yeast plasma membrane receptor signals its ligand-stimulated endocytosis. *Cell* **84**, 277-287 (1996).
8. L. Hicke, B. Zanolari, H. Riezman, Cytoplasmic tail phosphorylation of the alpha-factor receptor is required for its ubiquitination and internalization. *J Cell Biol* **141**, 349-358 (1998).
9. C. L. Jackson, J. B. Konopka, L. H. Hartwell, S. cerevisiae a pheromone receptors activate a novel signal transduction pathway for mating partner discrimination. *Cell* **67**, 389-402 (1991).
10. D. D. Jenness, P. Spatrick, Down regulation of the alpha-factor pheromone receptor in S. cerevisiae. *Cell* **46**, 345-353 (1986).

11. E. E. Bar, A. T. Ellicott, D. E. Stone, Gβγ recruits Rho1 to the site of polarized growth during mating in budding yeast. *J Biol Chem* **278**, 21798-21804 (2003).

12. L. C. Robinson, E. J. Hubbard, P. R. Graves, A. A. DePaoli-Roach, P. J. Roach, C. Kung, D. W. Haas, C. H. Hagedorn, M. Goebl, M. R. Culbertson, et al., Yeast casein kinase I homologues: an essential gene pair. *Proc Natl Acad Sci USA* **89**, 28-32 (1992).

13. G. M. Cole, D. E. Stone, S. I. Reed, Stoichiometry of G protein subunits affects the Saccharomyces cerevisiae mating pheromone signal transduction pathway. *Mol Cell Biol* **10**, 510-517 (1990).

14. M. Whiteway, I. Hougan, D. Y. Thomas, Overexpression of the STE4 gene leads to mating response in haploid Saccharomyces cerevisiae. *Mol Cell Biol* **10**, 217-222 (1990).

15. E. Draper, O. Dubrovskyi, E. E. Bar, D. E. Stone, Dse1 may control cross talk between the pheromone and filamentation pathways in yeast. *Curr Genet* **55**, 611-621 (2009).

16. G. M. Cole, S. I. Reed, Pheromone-induced phosphorylation of a G protein β subunit in S. cerevisiae is associated with an adaptive response to mating pheromone. *Cell* **64**, 703-716. (1991).

17. H. Flotow, P. R. Graves, A. Q. Wang, C. J. Fiol, R. W. Roeske, P. J. Roach, Phosphate groups as substrate determinants for casein kinase I action. *J Biol Chem* **265**, 14264-14269 (1990).

18. H. Flotow, P. J. Roach, Synergistic phosphorylation of rabbit muscle glycogen synthase by cyclic AMP-dependent protein kinase and casein kinase I. Implications for hormonal regulation of glycogen synthase. *J Biol Chem* **264**, 9126-9128 (1989).

19. F. Meggio, A. Donella-Deana, L. A. Pinna, Studies on the structural requirements of a microsomal cAMP-independent protein kinase. *FEBS Lett* **106**, 76-80 (1979).

20. E. Li, M. J. Cismowski, D. E. Stone, Phosphorylation of the pheromone-responsive Gβ protein of Saccharomyces cerevisiae does not affect its mating-specific signaling function. *Mol Gen Genet* **258**, 608-618 (1998).

21. R. DeFlorio, M. E. Brett, N. Waszczak, E. Apollinari, M. V. Metodiev, O. Dubrovskyi, D. Eddington, R. A. Arkowitz, D. E. Stone, Phosphorylation of Gβ is crucial for efficient chemotropism in yeast. *J Cell Sci* **126**, 2997-3009 (2013).

22. D. R. Ballon, P. L. Flanary, D. P. Gladue, J. B. Konopka, H. G. Dohlman, J. Thorner, DEP-domain-mediated regulation of GPCR signaling responses. *Cell* **126**, 1079-1093 (2006).

23. J. P. Howard, J. L. Hutton, J. M. Olson, G. S. Payne, Sla1p serves as the targeting signal recognition factor for NPFX(1,2)D-mediated endocytosis. *J Cell Biol* **157**, 315-326 (2002).

24. J. Y. Toshima, J. Nakanishi, K. Mizuno, J. Toshima, D. G. Drubin, Requirements for recruitment of a G protein-coupled receptor to clathrin-coated pits in budding yeast. *Mol Biol Cell* **20**, 5039-5050 (2009).

25. A. W. McClure, M. Minakova, J. M. Dyer, T. R. Zyla, T. C. Elston, D. J. Lew, Role of Polarized G Protein Signaling in Tracking Pheromone Gradients. *Dev Cell* **35**, 471-482 (2015).

26. J. B. Kelley, G. Dixit, J. B. Sheetz, S. P. Venkatapurapu, T. C. Elston, H. G. Dohlman, RGS proteins and septins cooperate to promote chemotropism by regulating polar cap mobility. *Curr Biol* **25**, 275-285 (2015).

27. K. R. Ayscough, D. G. Drubin, A role for the yeast actin cytoskeleton in pheromone receptor clustering and signalling. *Curr Biol* **8**, 927-930 (1998).

28. A. Sahin, B. Daignan-Fornier, I. Sagot, Polarized growth in the absence of F-actin in Saccharomyces cerevisiae exiting quiescence. *PLoS One* **3**, e2556 (2008).

29. F. O. Bendezu, S. G. Martin, Actin cables and the exocyst form two independent morphogenesis pathways in the fission yeast. *Mol Biol Cell* **22**, 44-53 (2011).

30. T. Yamamoto, J. Mochida, J. Kadota, M. Takeda, E. Bi, K. Tanaka, Initial polarized bud growth by endocytic recycling in the absence of actin cable-dependent vesicle transport in yeast. *Mol Biol Cell* **21**, 1237-1252 (2010).

31. B. Hegemann, M. Unger, S. S. Lee, I. Stoffel-Studer, J. van den Heuvel, S. Pelet, H. Koeppl, M. Peter, A Cellular System for Spatial Signal Decoding in Chemical Gradients. *Dev Cell* **35**, 458-470 (2015).

32. D. Matheos, M. Metodiev, E. Muller, D. Stone, M. D. Rose, Pheromone-induced polarization is dependent on the Fus3p MAPK acting through the formin Bni1p. *J Cell Biol* **165**, 99-109 (2004).

33. M. V. Metodiev, D. Matheos, M. D. Rose, D. E. Stone, Regulation of MAPK function by direct interaction with the mating-specific Gα in yeast. *Science* **296**, 1483-1486 (2002).

34. B. Errede, L. Vered, E. Ford, M. I. Pena, T. C. Elston, Pheromone-induced morphogenesis and gradient tracking are dependent on the MAPK Fus3 binding to Gα. *Mol Biol Cell*, Epub ahead of print (2015).

35. J. M. Dyer, N. S. Savage, M. Jin, T. R. Zyla, T. C. Elston, D. J. Lew, Tracking shallow chemical gradients by actin-driven wandering of the polarization site. *Curr Biol* **23**, 32-41 (2013).

36. T. I. Moore, C. S. Chou, Q. Nie, N. L. Jeon, T. M. Yi, Robust spatial sensing of mating pheromone gradients by yeast cells. *PLoS One* **3**, e3865 (2008).

37. T.-M. Yi, S. Chen, C.-S. Chou, Q. Nie, Modeling yeast cell polarization induced by pheromone gradients. *J Stat Phys* **128**, 193-207 (2007).

38. T. Jin, Gradient sensing during chemotaxis. *Curr Opin Cell Biol* **25**, 532-537 (2013).

39. Y. Wang, C. L. Chen, M. Iijima, Signaling mechanisms for chemotaxis. *Dev Growth Differ* **53**, 495-502 (2011).

40. C. L. Jackson, J. B. Konopka, L. H. Hartwell, S. cerevisiae [alpha] pheromone receptors activate a novel signal transduction pathway for mating partner discrimination. *Cell* **67**, 389-402 (1991).

41. L. Vallier, Jeffrey E. Segall Michael Snyder, The alpha-factor receptor C-terminus is important for mating projection formation and orientation in Saccharomyces cerevisiae. *Cell Motil Cytoskeleton* **53**, 251-266 (2002).

42. J. E. Segall, Polarization of yeast cells in spatial gradients of alpha mating factor. *Proc Natl Acad Sci USA* **90**, 8332-8336 (1993).

43. E. Blackwell, I. M. Halatek, H. J. Kim, A. T. Ellicott, A. A. Obukhov, D. E. Stone, Effect of the pheromone-responsive Gα and phosphatase proteins of Saccharomyces cerevisiae on the subcellular localization of the Fus3 mitogen-activated protein kinase. *Mol Cell Biol* **23**, 1135-1150 (2003).

44. F. van Hemert, M. D. Lazova, B. E. Snaar-Jagaska, T. Schmidt, Mobility of G proteins is heterogeneous and polarized during chemotaxis. *J Cell Sci* **123**, 2922-2930 (2010).

45. X. Xu, T. Meckel, J. A. Brzostowski, J. Yan, M. Meier-Schellersheim, T. Jin, Coupling mechanism of a GPCR and a heterotrimeric G protein during chemoattractant gradient sensing in Dictyostelium. *Sci Signal* **3**, 1-11 (2010).

46. J. A. Brzostowski, S. Sawai, O. Rozov, X. H. Liao, D. Imoto, C. A. Parent, A. R. Kimmel, Phosphorylation of chemoattractant receptors regulates chemotaxis, actin reorganization and signal relay. *J Cell Sci* **126**, 4614-4626 (2013).

47. F. M. Ausubel, R. Brent, R. E. Kingston, D. D. Moore, J. G. Seidman, J. A. Smith, K. Struhl, *Current Protocols in Molecular Biology*. K. Janssen, Ed., Current Protocols in Molecular Biology (John Wiley and Sons, Inc., 1994).

48. C. Guthrie, G. R. Fink, *Guide to Yeast Genetics and Molecular Biology.*, Methods Enzymol (Academic Press, San Diego, CA., 2002), vol. 351, pp. 325-456.

49. F. Sherman, G. R. Fink, J. B. Hicks, Eds., , *Laboratory Course Manual For Methods in Yeast Genetics*. (Cold Spring Harbor Laboratory Press, Cold Spring Harbor, New York, 1986).

50. S. I. Reed, J. A. Hadwiger, A. T. Lorincz, Protein kinase activity associated with the product of the yeast cell division cycle gene CDC28. *Proc. Natl. Acad. Sci. USA* **82**, 4055-4059 (1985).

51. A. Wach, PCR-synthesis of marker cassettes with long flanking homology regions for gene disruptions in S. cerevisiae. *Yeast* **12**, 259-265 (1996).

52. M. J. Cismowski, M. Metodiev, E. Draper, D. E. Stone, Biochemical analysis of yeast Gα mutants that enhance adaptation to pheromone. *Biochem Biophys Res Commun* **284**, 247-254 (2001).

53. R. Dunn, D. A. Klos, A. S. Adler, L. Hicke, The C2 domain of the Rsp5 ubiquitin ligase binds membrane phosphoinositides and directs ubiquitination of endosomal cargo. *J Cell Biol* **165**, 135-144 (2004).

54. Z. Tong, X. D. Gao, A. S. Howell, I. Bose, D. J. Lew, E. Bi, Adjacent positioning of cellular structures enabled by a Cdc42 GTPase-activating protein-mediated zone of inhibition. *J Cell Biol* **179**, 1375-1384 (2007).

55. R. D. Gietz, A. Sugino, New yeast-Escherichia coli shuttle vectors constructed with in vitro mutagenized yeast genes lacking six-base pair restriction sites. *Gene* **74**, 527-534 (1988).

56. I. Remy, A. Montmarquette, S. W. Michnick, PKB/Akt modulates TGF-beta signalling through a direct interaction with Smad3. *Nat Cell Biol* **6**, 358-365 (2004).

57. G. M. Cole, S. I. Reed, Pheromone-induced phosphorylation of a G protein [beta] subunit in S. cerevisiae is associated with an adaptive response to mating pheromone. *Cell* **64**, 703-716 (1991).

58. L. Alldridge, G. Metodieva, C. Greenwood, K. Al-Janabi, L. Thwaites, P. Sauven, M. Metodiev, Proteome profiling of breast tumors by gel electrophoresis and nanoscale electrospray ionization mass spectrometry. *J Proteome Res* **7**, 1458-1469 (2008).

59. M. V. Metodiev, Applications of nanoscale liquid chromatography coupled to Tandem mass spectrometry in quantitative studies of protein expression, protein-protein interaction, and protein phosphorylation. *Methods Mol Biol* **790**, 99-113 (2011).

60. G. Metodieva, N. C. Nogueira-de-Souza, C. Greenwood, K. Al-Janabi, L. Leng, R. Bucala, M. V. Metodiev, CD74-dependent deregulation of the tumor suppressor scribble in human epithelial and breast cancer cells. *Neoplasia* **15**, 660-668 (2013).

61. A. Vernay, S. Schaub, I. Guillas, M. Bassilana, R. A. Arkowitz, A steep phosphoinositide bis-phosphate gradient forms during fungal filamentous growth. *J Cell Biol* **198**, 711-730 (2012).

62. J. Y. Toshima, J. Toshima, M. Kaksonen, A. C. Martin, D. S. King, D. G. Drubin, Spatial dynamics of receptor-mediated endocytic trafficking in budding yeast revealed by using fluorescent alpha-factor derivatives. *Proc Natl Acad Sci USA* **103**, 5793-5798 (2006).

63. R. D. Gietz, A. Sugino, New yeast—Escherichia coli shuttle vectors constructed with in vitro mutagenized yeast genes lacking six-base pair restriction sites. *Gene* **74**, 527-534 (1988).

64. N. Paquin, M. Ménade, G. Poirier, D. Donato, E. Drouet, P. Chartrand, Local activation of yeast ASH1 mRNA translation through phosphorylation of Khd1p by the casein kinase Yck1p. *Mol Cell* **26**, 795-809 (2007).

65. T. M. Yi, H. Kitano, M. I. Simon, A quantitative characterization of the yeast heterotrimeric G protein cycle. *Proc Natl Acad Sci USA* **100**, 10764-10769 (2003).

66. C. S. Chou, Q. Nie, T. M. Yi, Modeling robustness tradeoffs in yeast cell polarization induced by spatial gradients. *PLoS One* **3**, e3103 (2008).

67. C. I. Maeder, M. A. Hink, A. Kinkhabwala, R. Mayr, P. I. Bastiaens, M. Knop, Spatial regulation of Fus3 MAP kinase activity through a reaction-diffusion mechanism in yeast pheromone signalling. *Nat Cell Biol* **9**, 1319-1326 (2007).

68. S. Ghaemmaghami, W. K. Huh, K. Bower, R. W. Howson, A. Belle, N. Dephoure, E. K. O'Shea, J. S. Weissman, Global analysis of protein expression in yeast. *Nature* **425**, 737-741 (2003).

Acknowledgments: We thank D. King for the generous gift of Alexa Fluor 594-conjugated α-factor. Supported by NSF grants 1024718 and 1415589 (DES), CNRS grant PICS06228 and Fondation ARC grant SFI20121205755 (RA), NIH grant GM079804 and NSF grant DBI 1062328 (JL), and NIH grant 1RO3CA150131 (MVM). This work was also funded by the Chicago Biomedical Consortium with support from the Searle Funds at The Chicago Community Trust.

FIGURES AND TABLES

Figure 1. Physical and genetic interaction between Gβ and Yck1/2. **(A)** Binding of Yck1-myc to Gβγ and $G\beta^{P}$-γ affinity beads. H and L indicate high and low input of lysate containing Yck1-myc, respectively. In the control lanes, the beads were not loaded with G protein.

(B) Immunoblot quantification of Yck1 pull-down by Gβγ-affinity beads. The absolute intensity (AI) of the myc-Yck1 bands in the low input lanes of the immunoblot shown in Fig. 1A was measured using ImageJ. The signal above noise (SAN) for myc-Yck1 was calculated by subtracting the negative control (empty) AI from the Gβγ and $G\beta^{P-}\gamma$ AI. The relative amount of myc-Yck1 binding to Gβγ vs. $G\beta^{P-}\gamma$ is expressed as the $G\beta/G\beta^{P-}$ ratio. This blot is representative of three trials. **(C)** Gβ-Yck1 interaction was visualized in pheromone-treated cells prior to morphogenesis (top) and after mating projection formation (bottom) using BiFC. Some fluorescence was detectable at the tips of shmooing negative control cells (bottom middle), but this was of lower intensity and distinct localization compared to that in the experimental cells (see Table 2). **(D)** Western blot analysis of *yck1*Δ *yck2*^{ts} cells assayed for pheromone-induced phosphorylation of Gβ at the permissive and restrictive temperatures. **(E)** Phospho-map of Gβ 317-337 region. Blue and green indicate sites identified by mass spec analysis only (see Fig. S1) and genetic analysis only (*20*), respectively; Red indicates sites identified by both methods. Arrows indicate putative MAPK and CK1 sites.

Figure 2. Effect of Gβ and $G\beta^{P-}$ on receptor phosphorylation. **(A-C)** Gβ but not $G\beta^{P-}$ overexpression inhibits receptor phosphorylation. (A) Representative images of cells expressing the native level of Gβ, excess Gβ, or excess $G\beta^{P-}$, treated with pheromone and latA at time 0. The intensity of the Sst2-GFP signal on the PM corresponds to the location and quantity of unphosphorylated receptor. The intensity of the $Ste2^{7XR}$-mCherry signal corresponds to the location and quantity of all receptor. The arrowhead indicates a polarized Sst2-GFP crescent. ↑↑ indicates overexpression. (B) Immunoblot showing relative amounts of Gβ and $G\beta^{P-}$ after 0 and 2 hours of *GAL1*-indution. The highest MW

band is Gβ; the asterisks indicate Gβ degradation products. (C) Normalized quantification of Sst2-GFP localization to the PM. The relative PM localization of Sst2-GFP was normalized to receptor expression by dividing the mean PM Sst2-GFP signal by the mean PM Ste2^{7XR}-mCherry signal. The graph shows the mean ratios ± SEM at the indicated time points. t-test *p* values were calculated relative to the control. *$p \leq 0.003$. Three trials were conducted with the control and Gβ overexpressing strains ($n \geq 44$ for each strain and time point); two trials were conducted with the Gβ^{P-} overexpressing strain ($n = 15$ for each time point). (**D** and **E**) Gβ overexpression augments phospho-receptor polarity in pheromone- and latA-treated cells. (D) Representative images of cells expressing the native level of Gβ, excess Gβ, or excess Gβ^{P-}, treated with pheromone and latA at time 0. (E) The degree of Sst2-GFP polarization on the PM of each cell is indicated by the Polarity Index (PI), which was determined by dividing the mean fluorescence on the brightest 1/3rd of the PM by the mean signal on the rest of the PM. The graph shows the mean PIs ± SEM. t-test *p* values were calculated relative to Gβ↑↑. *$p < 0.02$; **$p = 0.002$; †$p = 0.0003$; $n \geq 20$ for each strain and time point. At least two trials were conducted with each strain. (**F** and **G**) The receptor is hyper-phosphorylated in Gβ^{P-} cells. (F) Representative images of cells expressing the native levels of Gβ and Gβ^{P-}, treated with pheromone and latA at time 0. (G) Quantification of Sst2-GFP localization to the PM. The graph shows the mean PM GFP values ± SEM. t-test *$p = 0.005$; $n = 15$ for each strain and time point. PM Ste2^{7XR}-mCherry levels did not differ significantly in the control and experimental cells.

Figure 3. Independent effects of receptor phosphorylation and internalization on chemotropism. Time-lapse images of mating cells showing the Sst2-GFP reporter relocating from the

presumptive default polarity site to the presumptive chemotropic site. The degree of movement is described by the orientation angle, δ (yellow arc). Comparing control to $G\beta^{P-}$ cells, the mean orientation angles ± SEM were 82.6 ± 8.0 vs. 52.0 ± 8.4 (t-test $p = 0.01$; $n \geq 33$.) Two trials were conducted with each strain.

Figure 4. Effects of receptor internalization and phosphorylation on chemotropism.

(A) Orientation and fusion angle measurements. Cartoons illustrating how the initial orientation angles (left, δ) and the fusion angles (right, γ) were measured. Polarized growth initiated within 45˚of the cytokinesis site (CKS, red bar) was presumed to be at the default polarity site, demarcated by the dotted blue lines. (B) Time-lapse DIC and fluorescent images of mating mixtures taken at 15-minute intervals. Measurements reported in panels C-F were performed exclusively on *MAT***a** cells whose CKS could be identified and which were initially within 1 μm of their eventual mating partner. The GFP-Bud1 PM signal was used to distinguish the *MAT*α cells and as a marker for cell fusion. Fluorescent images show the mating cells at the first time point, and at the time points immediately before and after fusion. The initial orientation, reorientation, and fusion angles are indicated by δ, δ', and γ, respectively. i. Representative WT X WT mating showing the direct orientation of the mating partners toward one another, formation of mating projections within 15 min, cell fusion within 45 min, and the resulting symmetrical zygote. The *MAT*α cell shmooed opposite its CKS; ii. Example of a mating cell reorienting by initiating a second projection in a WT X WT cross; iii. Representative WT *MAT*α X *MAT***a** $STE2^{7XR}$ mating showing defective initial orientation and the formation of an angled zygote after 90 min; iv. Two representative WT *MAT*α X *MAT***a** $STE2^{7XR\ 6SA}$ matings showing a *MAT*α cell fusing adjacent to the

CKS of a mutant cell that failed to polarize its growth (top), and a mutant cell that broadly polarized its growth in the default region, but failed to fuse with an adjacent partner until it had elongated over an abnormally long time and distance (bottom); v. Two representative WT *MAT*α X *MAT***a** *STE2*$^{7XR\ 6SD}$ matings showing mutant cells that broadly polarized their growth at the default site (top), or presumptive default site (bottom), and elongated while persistently turning until their growth zones were apposed to a partner. In each case, the mutant cell could have mated more efficiently by switching to a chemotropic growth site: In the first example, a 180˚ switch would have resulted in a 0˚ fusion angle with the eventual partner; In the second example, initiation of a second polarization site directed toward the nearest partner (yellow *MAT*α), as is observed in WT mating mixtures (above), would have resulted in considerably earlier fusion.
(C) Quantification of initial orientation angles. Initial orientation angles (purple lines) were measured as shown in panel A (left) and compared by t-test. *$p < 0.06$; **$p = 0.003$; ***$p < 0.0001$. (D) Quantification of fusion angles. Fusion angles (aqua lines) were measured as shown in panel A (right) and compared by t-test. *$p < 0.0001$. (E) Time to fusion. Diffusion of GFP-Bud1 from the *MAT*α partner to the *MAT***a** partner was used as a marker for the completion of cell fusion. The time-to-fusion data for each *MAT***a** strain was compared by t-test. *$p = 0.01$; **$p < 0.0001$. (F) Effect of receptor mutants on morphogenesis. *MAT***a** cells that mated were placed in three classes based on their ability to form mating projections: tapered growth (normal shmoos), broadly polarized growth, and no polarized growth. The proportion of normal shmoos was compared by chi-square test. *$p < 0.0001$.

Figure 5. Localization of receptor and Cdc42-GTP reporters in vegetative and pheromone-stimulated G1 cells. **(A** and **B)** Sequential polarization of the receptor and active Cdc42 in cultured cells. Strain AIY301 was grown to log-phase, and G1 (round, unbudded) cells were scored for polarization of the Ste2-GFP (receptor) and Gic2-PBD-RFP (Cdc42-GTP) reporters before and after pheromone treatment. (A) Representative images 60 min after treatment with pheromone. The exposures and processing were the same for all images. (B) Relative proportions of cells showing Ste2-GFP and the Gic2-PBD-RFP polarity before and after pheromone-induced morphogenesis. RNP = round cell, neither reporter polarized; RAC = round cell, activated Cdc42 polarized; RR = round cell, receptor reporter polarized; RB = round cell, both reporters polarized; SB = shmooing cell, both reporters polarized. The x-axis indicates time after pheromone treatment. n = 20, 35, and 56 at the 0, 1, and 2 hour time points, respectively. **(C** and **D)** Sequential polarization of the receptor and active Cdc42 in mating cells. (C) Proportion of cells that show sequential re-localization of the Ste2-GFP and Gic2-PBD-RFP reporters in mating mixtures. Time of Polarity Switch (PS) is defined as the time a reporter has stably re-localized to the future growth site, and corresponds to the solid arrowheads in panel D (n = 19); Time of Polarity Fixed (PF) is defined as the time a reporter has fully re-localized to the future growth site, and corresponds to the filled arrowheads in panel D (n = 16). (D) Time-lapse images of representative *MAT***a** cells that switch from their presumptive default polarity site to a presumptive chemotropic growth site in mating mixtures. Polarity of the Ste2-GFP and Gic2-PBD-RFP reporters is categorized in one of three ways: established at the initial site (dotted arrowheads), established at the final site (solid arrowheads), and fully switched to the final site (filled arrowheads). The exposures

were the same for all images. Processing was the same for all Ste2-GFP images in a given series, and all Gic2-PBD-RFP in a given series.

Figure 6. Effect of $G\beta^{P-}$ on receptor polarization. **(A** and **B)** Isotropic conditions. Gβ and $G\beta^{P-}$ cells expressing the receptor reporter, Ste2-GFP, were treated with pheromone at time 0 and with latA after global receptor internalization (15'). (A) Representative images. Arrowheads indicate Ste2-GFP crescents. (B) Polarity Indices were measured as in Fig. 2D and compared by t-test. The graph shows mean PIs ± SEM representing three trials for each strain. $*p < 0.03$; $n \geq 30$ for each strain and time point. **(C** and **D)** Mating mixtures. (C) Time-lapse images of mating Gβ and $G\beta^{P-}$ cells showing Ste2-GFP localization. Insets show BudPolarity output (*61*). (D) Receptor polarization was quantified by dividing the peak by the minimum PM fluorescence prior to apparent morphogenesis. The mean polarization values ± SEM were 1.76 ± 0.14 and 1.28 ± 0.07 for Gβ and $G\beta^{P-}$ cells, respectively. t-test $p < 0.007$; $n \geq 17$. Two trials were conducted with each strain.

Figure 7. Proposed feedback loops that drive receptor polarization upstream of directed secretion. **(A)** Cartoon depiction of the model. We propose that the establishment of pheromone-induced cell polarity prior to the initiation of actin-cable directed secretion depends on two interconnected positive feedback loops. Initially, a shallow gradient of pheromone is mirrored by a similarly shallow gradient of occupied receptor across the cell. This slight differential in activated receptor leads to a corresponding differential in activated G protein. Gα recruits the Fus3 MAPK to phosphorylate Gβ (loop 1), which augments its interaction with Yck1/2 while preventing its interaction with Gα. As $G\beta^{P}\gamma$ inhibits receptor internalization by interacting with Yck1/2, the signaling apparatus

preferentially accumulates on the up-gradient side of the cell (loop 2). The two loops act synergistically to promote local signaling while protecting $G\beta^{P}\gamma$ from internalization, thereby generating a concentration gradient of free $G\beta^{P}\gamma$. Ultimately, the localized increase in Gβγ is sufficient to trigger the nucleation of actin cables. Directed secretion then reinforces the spatial signal and drives mating projection formation. **(B-D)** Network diagrams. (B) Network 1. Yck1/2 (Yck) triggers the internalization of inactive and active receptors (R, RL), represented by the blue and green bars, respectively. One heterotrimeric G protein is removed along with each receptor. (C) Network 2. Phosphorylation of Gβ and $G\beta^{P}\gamma$-Yck interaction are included. The binding of $G\beta^{P}\gamma$ (GbgP) to Yck inhibits receptor and G protein internalization. (D) Network 3. The Gα-Fus3 feedback loop is included. Active Gα recruits active Fus3 to phosphorylate Gβ, which augments the interaction of Gβ with Yck and Gβγ-activation of Fus3 through the MAPK cascade (not shown). **(E-G)** Comparison of network output. The graphs show the spatio-temporal dynamics of the total receptor (both active and inactive). (E) Network 1. Without downstream regulation, the pheromone gradient induces complete removal of the receptor from the membrane; no polarity is generated. (F) Network 2. With the addition of $G\beta^{P}\gamma$-Yck interaction, which slows receptor and G protein internalization, the pheromone gradient induces receptor polarity. (G) Network 3. Gα recruitment of Fus3 leads to locally enhanced phosphorylation of Gβ, and consequently, faster receptor polarization.

Figure S1. Examples of mass spectra used to map the sites of pheromone-induced Gβ phosphorylation. Samples prepared from vegetative cells overexpressing Gβγ in normal medium and pheromone-treated cells overexpressing Gβγ in heavy medium were

analyzed together by mass spectrometry to identify sites of pheromone-induced Gβ phosphorylation. The diagnostic fragment ions are indicated by arrowheads. **(A)** Collision-induced dissociation (CID) spectrum of a doubly-phosphorylated peptide locating the phosphates at S335 (for certain) and either of T318 or T320. The diagnostic fragment ions for S335 are y_5 and y_6, and for S318/S320 is b_3. The Andromeda score is 110. **(B)** High-resolution high-collision energy dissociation spectrum (HCD) of the singly-phosphorylated peptide locating the phosphate at T320. The diagnostic ions are b_2 and b_3. The Andromeda score is 116. **(C)** CID spectrum of a doubly-phosphorylated peptide locating the phosphates at T318 and T320. The diagnostic fragment ions are b_5, b_6, and b_8. The Andromeda score is 115. **(D)** HCD spectrum of the singly-phosphorylated peptide locating the phosphate at T320. The diagnostic fragment ions are b_2 and b_3. The Andromeda score is 81.

Figure S2. Dynamic localization of the pheromone receptor as cells orient toward mating partners. *MAT***a** cells expressing an endogenously tagged α-factor receptor, Ste2-GFP, were mixed with *MAT*α cells and incubated at 30˚C for the indicated times. Arrowheads indicate localization of the receptor to the default polarity site; Arrows indicate redistribution of the receptor to the chemotropic site before morphogenesis. The cell pictured in the lower rows formed a zygote with the indicated *MAT*α cell between the 60 and 75 minute time points.

Figure S3. Exogenous pheromone induces formation of angled zygotes. WT strains DSY257 (*MAT***a** *bar1*Δ) and DSY129 (*MAT*α *bar1*Δ) were mated for up to 4 hours on standard plate medium and on medium containing 60 nM pheromone. Fusion angles were measured as shown in Fig. 4A and compared by t-test. $*p = 0.0003$; $n \geq 46$.

Figure S4. Time-lapse images of elongating and turning *MAT***a** *STE2*$^{7XR\ 6SA}$ and *MAT***a** *STE2*$^{7XR\ 6SD}$ cells in mating mixtures. Additional images from the experiments represented in Fig. 4. **(A-B)** Examples of mutant cells responsive to pheromone, but apparently unable to orient in response to pheromone gradients. **(A)** A *MAT***a** *STE2*$^{7XR\ 6SA}$ cell broadly polarizes its growth away from a group of WT *MAT*α cells, persistently turning as it elongates, but failing to mate after 270 min. **(B)** A *MAT***a** *STE2*$^{7XR\ 6SD}$ cell broadly polarizes its growth away from WT *MAT*α cells with which it is in contact, persistently turning as it elongates, but failing to mate after 360 min.

Figure S5. Surface distribution of receptor assayed by Alexa Fluor 594-conjugated α-factor binding. **(A)** Alexa Fluor 594-conjugated α-factor binds specifically to the Ste2 pheromone receptor. Wild type (DSY257) and *ste2*Δ (EDY208) cells were stained with labeled α-factor and imaged as described in the Materials & Methods. **(B)** Alexa Fluor 594-conjugated α-factor reveals receptor on the surface of cells in which Ste2-GFP is not detectable. Samples of vegetative and pheromone-stimulated cells expressing Ste2-GFP (DMY169) were treated with sodium azide at the indicated times and either imaged at 488 nm (top), or stained with Alexa Fluor 594-conjugated α-factor, and imaged at 561 nM (bottom).

Figure S6. Receptor internalization assay. **(A)** Time-lapse images of a cell internalizing receptors bound to Alexa Fluor 594-conjugated α-factor. The arrowheads indicate internalized label. **(B)** Line graphs showing the change in PM fluorescence over time with the high frequency noise filtered out for the cell shown in panel A. The decay rate represents the change in PM fluorescence around the cell from the first to last time point, with white denoting no loss of signal and dark blue corresponding to complete loss. The

pink box and black bar indicate the putative protected region. **(C)** The graph represents the average rate of PM signal decay for the front and back of cells that exhibited a discrete region of the PM with a significantly slower rate of signal loss than the remainder of the PM (n = 12). The area of "receptor protection" was defined as the points in the 30th percentile for decay rate (blue line); the remainder of the PM was defined as "unprotected" (green line). Error bars = SEM.

Figure S7. Spatial model of the computational yeast cell. The cell of radius r was discretized into n latitude bands and each latitude band was cut into m patches. In this study, n = 16 and m = 40. Molecules in the "pizza slices" around the poles diffuse among the three neighboring patches; molecules in other patches diffuse among the four neighboring patches**.**

Figure S8. Computational model of receptor dynamics. Output from Networks 1-3 is shown from left to right. **(A)** Rate of receptor internalization. In Network 1, without downstream regulation, the rate of receptor internalization decreases uniformly as the number of receptors on the PM decreases. In Network 2, receptor interaction starts off faster on the up-gradient side of the cell, but this difference inverts within 15 min as $G\beta^{P}\gamma$ inhibits Yck. In Network 3, receptor internalization becomes slower on the up-gradient side of the cell within 12 min as Gα recruitment of Fus3 locally enhances phosphorylation of Gβ. **(B)** Localization of activated receptor. The activated receptor does not polarize in Network 1, but polarizes robustly in Network 2. It polarizes to similar degree in Network 3, but about 3 min faster.

Figure S9. Computational model of G protein dynamics. Output from Networks 1-3 is shown from left to right. No polarity is generated in Network 1, nor does the

heterotrimeric G protein polarize significantly in Networks 2 or 3. However, activated Gα steadily accumulates on the up-gradient side of the cell, while its level remains constant on the opposite side in these networks. In contrast, total free Gβγ undergoes a precipitous drop, partially due to the interaction of $G\beta^{P}\gamma$ with Yck, before recovering and becoming highly concentrated on the up-gradient side. Free $G\beta^{P}\gamma$ ultimately becomes the most polarized component, reaching a level 2 times (Network 2) and 3 times (Network 3) greater than that of Gβγ in a small region of the cell surface. **(A)** Heterotrimeric G protein. **(B)** Activated Gα. **(C)** Total free Gβγ (unphosphorylated and phosphorylated). **(D)** Free Gβγ. **(E)** Free $G\beta^{P}\gamma$.

Figure S10. Computational model of Yck dynamics. Output from Networks 1-3 is shown from left to right. The time axes are plotted in opposite directions in panels A and B.

In Network 1, Yck is unregulated, and therefore, unaffected by the gradient. In Networks 2 and 3, free Yck concentrates to the back side of the cell while Yck-$G\beta^{P}\gamma$ concentrates to the front side of the cell. **(A)** Distribution of free Yck. **(B)** Distribution of $G\beta^{P}\gamma$-bound Yck.

Detected Protein	Affinity Beads	Intensity 70-55 kDa	Intensity 55-45 kDa	Total Intensity	Gβ/Gβ^{P-} ratio
Yck1	Gβγ	3.16E+07	2.25E+07	5.42E+07	2.25
	Gβ^{P-}γ	6.88E+06	1.72E+07	2.41E+07	
	Empty	0	0	0	
Yck2	Gβγ	2.39E+07	0	2.39E+07	2.09
	Gβ^{P-}γ	1.15E+07	0	1.15E+07	
	Empty	0	0	0	

Table 1. Mass spec quantification of Yck1 and Yck2 pull-down by Gβγ-affinity beads. 225 μg of total protein (low input) from cells expressing the native level of Yck2 and overexpressing myc-Yck1 were incubated with Gβγ-affinity and negative control beads. Bound proteins were separated by PAGE, processed, and analyzed by mass spec as described in the Materials & Methods.

	% cells with PM signal[a]		PM/Cyto ± SEM[b]		% PM ± SEM ≥ 1.25X Cyto[c]	
	Pre-shmoo	Shmooed	Pre-shmoo	Shmooed	Pre-shmoo	Shmooed
Gβ-VF2 + VF1-Yck1	28.5	15.2	n.d.	1.46 ± 0.09*	n.d.	50.5 ± 5.4*
Gβ-VF2 + VF1	3.4	27.4	n.d.	0.95 ± 0.03	n.d.	17.0 ± 1.9

Table 2. Quantification of BiFC results. No background signal was seen in the Gβ-VF2+VF1 negative control cells. Detectable fluorescence was observed on the tips of a significant fraction of the shmooing Gβ-VF2 +VF1 negative control cells. This is attributable to the direct, irreversible interaction between the VF1 and VF2 fragments, where they are concentrated together by directed secretion, and is clearly distinguishable from the Gβ-VF2/VF1-Yck1 interaction signal by the measures shown here. [a]Cells with clear PM signal were scored; $n \geq 45$. [b]The PM signal was normalized to the cytoplasmic signal in each cell by dividing the mean PM fluorescence by the mean cytoplasmic fluorescence. [c]The fraction of the PM showing a signal at least 25% greater than the mean cytoplasmic signal in each cell was determined. *As compared to the corresponding measure for Gβ-VF2 + VF1 cells, $p < 0.0001$ ($n \geq 19$).

Table S1: Yeast strains used in this study

Strain	Background	Genotype	Reference
DSY257	BF264-15D	*MAT***a** *bar1*Δ *ade1 his2 leu2-3,112 trp1-1a ura3*Δ	Stone lab
DMY224		*MAT***a** *his3 leu2 ura3-52 STE2-GFP::LEU2*	(*6*)
DMY222		*MAT***a** *his3 leu2 ura3-52 yck1-D1::ura3 yck2-2^{ts} STE2-GFP::LEU2*	(*6*)
AIY100	BY4741	*MAT***a** *SST2-GFP-KanMX6 ste2^{7XR}-mCherry-caURA3 Gpa1^{G302S}*-HisMX6 YCplac111	This study
AIY101	BY4741	*MAT***a** *SST2-GFP-KanMX6 ste2^{7XR}-mCherry-caURA3 gpa1^{G302S}-HisMX6* YCplac111/GAL1-Ste4	This study
AIY221	BY4741	*MAT***a** *SST2-GFP-KanMX6 ste2^{7XR}-mCherry-caURA3 gpa1^{G302S}-HisMX6* ste4$^{T320A\ S335A}$(int.)::*LEU2*	This study
AIY109	BY4741	*MAT***a** *SST2-GFP-KanMX6 ste2^{7XR}-mCherry-*	
AIY164	BY4741	*caURA3 gpa1^{G302S}-HisMX6* YCplac111/GAL1-ste4$^{T320A\ S335A}$	Deletion library strain
YDB111	BY4741	*MAT***a** *his3*Δ1 *leu2*Δ0 *met15*Δ0 *ura3*Δ0 *ste4*Δ::*KanMX4* *MAT***a** *SST2-GFP-KanMX6 ste2^{7XR}-mCherry-caURA3 gpa1^{G302S}-HisMX6*	(*22*)
DMY169	BF264-15D	*MAT***a** *bar1*Δ *ade1 his2 leu2-3,112 trp1-1a ura3*Δ *STE2-GFP::LEU2*	(*6*)

AIY197	BF264-15D	*MAT***a** *ste4*$^{T320A\ S335A}$ *bar1*Δ *ade1 his2 leu2-3,112 trp1-1a ura3*Δ *STE2-GFP::LEU2*	This study
RDY114	BF264-15D	*MAT***a** *ste4*$^{T320A\ S335A}$ *bar1*Δ *ade1 his2 leu2-3,112 trp1-1a ura3*Δ	(*21*)
DSY246	BF264-15D	*MAT*α *bar1*Δ *ade1 his2 leu2-3,112 trp1-1a ura3*Δ	Stone lab
AIY273	BF264-15D	*MAT***a** *bar1*Δ *ade1 his2 leu2-3,112 trp1-1a ura3*Δ *ste7*Δ*::KanMX* YCplac22/GAL1-Ste7 pRS416/ADH1-VF1-Yck1 pRS415/ADH1-Ste4-VF2	This study
AIY276	BF264-15D	*MAT***a** *bar1*Δ *ade1 his2 leu2-3,112 trp1-1a ura3*Δ *ste7*Δ*::KanMX* YCplac22/GAL1-Ste7 pRS416/ADH1-VF1-Yck1 pRS415/ADH1-VF2	This study
AIY275	BF264-15D	*MAT***a** *bar1*Δ *ade1 his2 leu2-3,112 trp1-1a ura3*Δ *ste7*Δ*::KanMX* YCplac22/GAL1-Ste7 pRS415/ADH1-Ste4-VF2 pRS416/ADH1-VF1	This study
RDY126	BF264-15D	*MAT***a** *ste4::URA3 GFP-STE4::ura3 bar1*Δ *ade1 his2 leu2-3,112 trp1 ura3*Δ	(*21*)
NWY069	BF264-15D	*MAT***a** *bar*Δ *ste4*$^{T320A\ S335A}$ Δ*ste18::URA3 Δarg5/6::G418* Δ*lys1::hph ade1 his2 leu2-3,112 trp1-1a ura3*Δ YCplac22/GAL1-3xHA-Ste18	This study

		YCplac111/GAL1-ste4$^{T320A\ S335A}$	
NWY068	BF264-15D	*MAT***a** *bar*Δ Δ*ste18::URA3* Δ*arg5/6::G418* Δ*lys1::hph ade1 his2 leu2-3,112* *trp1-1a ura3*Δ YCplac22/GAL1-3xHA-Ste18 YCplac111/GAL1-Ste4	This study
NWY071	BF264-15D	*MAT***a** *bar*Δ Δ*ste18::URA3* Δ*arg5/6::G418* Δ*lys1::hph ade1 his2 leu2-3,112* *trp1-1a ura3*Δ YCplac22 YCplac111	This study
NWY074	BF264-15D	*MAT***a** *bar*Δ *ste4$^{T320A\ S335A}$* Δ*ste18::URA3* Δ*arg5/6::G418* Δ*lys1::hph ade1 his2 leu2-3,112 trp1-1a ura3*Δ YCplac22 YCplac111	This study
NWY073	BF264-15D	*MAT***a** *bar1*Δ *ade1 his2 leu2-3,112* *trp1-1a ura3*Δ pESC-LEU/GAL1-myc-Yck1	This study
NWY052	BF264-15D	*MAT***a** *bar1*Δ Δ*ste18::URA3* Δ*lys1::hph* *Δarg5/6::G418 ade1 his2 leu2-3,112* *trp1-1a ura3*Δ YCplac22/GAL1-His6x-Ste18 YCplac111/GAL1-Ste4	This study
EDY208	BF264-15D	*MAT***a** *bar1*Δ *ade1 his2 leu2-3,112* *trp1-1a ura3*Δ *ste2*Δ::*KanMX* #1a	Stone lab
DSY129	BF264-15D	*MAT*α *ade1 his2 leu2-3,112* *trp1-1a ura3*Δ	Stone lab
XWY005	BF264-15D	*MAT***a** *ade1 his2 leu2-3,112* *trp1-1a ura3*Δ *ste2$^{7XR\text{-}GPAAD}$::URA3*	This study
XWY027	BF264-15D	*MAT*α *ade1 his2 leu2-3,112*	This study

		*trp1-1a ura3*Δ pRS406/GFP-BUD1	
XWY008	BF264-15D	*MAT***a** *ade1 his2 leu2-3,112 trp1-1a ura3*Δ *ste2*$^{6SA\text{-}7XR\text{-}GPAAD}$*::URA3*	This study
XWY018	BF264-15D	*MAT***a** *ade1 his2 leu2-3,112 trp1-1a ura3*Δ *ste2*$^{6SD\text{-}7XR\text{-}GPAAD}$*::URA3*	This study
AIY301	BF264-15D	*MAT***a** *bar1*Δ *ade1 his2 leu2-3,112 trp1-1a ura3*Δ *STE2-GFP::LEU2 GIC2-PBD-RFP::URA3*	This study
RDY102	BF264-15D	*MAT***a** *bar1*Δ *ade1 his2 leu2-3,112 trp1-1a ura3*Δ ste4Δ::URA3	Stone lab
XWY011	BF264-15D	*MAT***a** *bar1*Δ *ade1 his2 leu2-3,112 trp1-1a ura3*Δ YCplac111/GAL1-Ste4	This study
XWY033	BF264-15D	*MAT***a** *bar1*Δ *ade1 his2 leu2-3,112 trp1-1a ura3*Δ YCplac111/GAL1-ste4$^{T320A\ S335A}$	This study

Table S2: Plasmids used in this study

Plasmid #	Plasmid name	Plasmid marker/type	Reference
MCB26	YCplac111/GAL1-Ste4	LEU2/CEN	(*52*)
DMB115	YCplac22-GAL1-myc-Yck1	TRP1/CEN	This study
DMB114	pESC-LEU/GAL1-myc-Yck1	LEU2/2μm	This study
RDB131	YCplac111/GAL1-ste4$^{I320A\ S335A}$	LEU2/CEN	(*21*)
NWB032	YCplac22/GAL1-3xHA-Ste18	TRP1/CEN	This study
AIB130	YIplac128/ste4$^{I320A\ S335A\ N\Delta112}$	LEU2/INT	This study
DSB155	YCplac111	LEU2/CEN	(*63*)
DSB156	YCplac33	URA3/CEN	(*63*)
DSB157	YCplac22	TRP1/CEN	(*63*)
LHP1921	Ste2$^{1-419}$-GFP	LEU2/INT	(*52*)
p416-VF1	pRS416/ADH1-Venus Fragment 1	URA3/2μm	(*56*)
p415-VF2	pRS415/ADH1-Venus Fragment 2	LEU2/2μm	(*56*)
pPC2	pRS416/ADH1-VF1-Yck1	URA3/2μm	(*64*)
AIB201	pRS415/ADH1-Ste4-VF2	LEU2/2μm	This study
MCB40	YCplac22/GAL1-His6x-Ste18	TRP1/CEN	(*52*)
	YIp211/Gic2-PBD-RFP	URA3/INT	(*54*)
DLB3850	pRS306/STE2$^{(600-1296)-7XR-GPAAD-3'UTR}$	URA3/INT	Lew lab
DLB3784	pRS306/STE2$^{(600-1296)-6SA-7XR-GPAAD-3'UTR}$	URA3/INT	Lew lab
DLB3851	pRS306/STE2$^{(600-1296)-6SD-7XR-GPAAD-3'UTR}$	URA3/INT	Lew lab
	pRS406/GFP-BUD1	URA3/INT	Arkowitz lab

Eq #	Equation	Comments
1	$h_v = \frac{\pi r}{n}$	Latitudinal patch spacing
2	$h_{ih} = r\sqrt{1-\cos^2(\frac{2i+1}{2n}\pi)}$	Longitudinal patch spacing
3	$x_{ij} = \sqrt{r^2 - z_{ij}^2}\cos(\frac{2j+1}{2m}2\pi), y_{ij} = \sqrt{r^2 - z_{ij}^2}\sin(\frac{2j+1}{2m}2\pi)$ and $z_{ij} = r\cos(\frac{2i+1}{2n}\pi)$	The position of the $\{i,j\}$-patch, (x_{ij}, y_{ij}, z_{ij})
4	$[\mathrm{L}(x_{ij})] = [\mathrm{L}(r)] + (x_{ij} - r)\cdot\psi$	pheromone concentration of the $\{i,j\}$-patch; $\psi = 1.25nM/\mu m$
5	$D\nabla^2[S_k(i,j)] = D(\frac{[S_k(i-1,j)] + [S_k(i+1,j)] - 2[S_k(i,j)]}{h_v^2} + \frac{[S_k(i,j-1)] + [S_k(i,j+1)] - 2[S_k(i,j)]}{h_{ih}^2})$	Diffusion of the k-th molecular species Sk in the $\{i,j\}$-patch[a]
6	$D\nabla^2[S_k(1,j)] = D(\frac{[S_k(1,j)] + [S_k(3,j)] - 2[S_k(2,j)]}{h_v^2} + \frac{[S_k(1,j-1)] + [S_k(1,j+1)] - 2[S_k(1,j)]}{h_{1h}^2})$	Diffusion of the k-th molecular species Sk in the patches ringing the north pole[a]
7	$D\nabla^2[S_k(n,j)] = D(\frac{[S_k(n,j)] + [S_k(n-2,j)] - 2[S_k(n-1,j)]}{h_v^2} + \frac{[S_k(n,j-1)] + [S_k(n,j+1)] - 2[S_k(n,j)]}{h_{nh}^2})$	Diffusion of the k-th molecular species Sk in the patches ringing the south pole[a]

Table S3. Equations used for spatial model of yeast cell. [a] $D = 0.001\mu m^2/s$ was used for all molecular species.

Parameter	Description	Initial Value	Reaction Rate [a]	Value
r	Cell radius	2μm	k_{rs}	$7.96 \times 10^{-2}\mu m^{-2}s^{-1}$ (*65*)
sa	Cell surface area	$50.27\mu m^2$	k_{rl}	$3.32 \times 10^{-3}\mu m^3 s^{-1}$ (*65*)
v	Cell volume	$33.51\mu m^3$	k_{rlm}	$0.01 s^{-1}$ (*65*)
L(r)	Pheromone at cell front	10nM	k_{gs}	$7.96 \times 10^{-2}\mu m^{-2}s^{-1}$
L(-r)	pheromone at cell back	5nM	k_{ga}	$5.03 \times 10^{-4}\mu m^2 s^{-1}$ (*65*)
R	Inactive receptor	10,000/sa (*10*)	k_{gad}	$0.11 s^{-1}$ (*65*)
RL	Active receptor	0	k_{gd}	$50.3\mu m^2\ s^{-1}$ (*65*)
G	Heterotrimeric G protein	10,000/sa (*10*)	k_{i0}	$5.03 \times 10^{-6}\mu m^2 s^{-1}$ (*65*)
Ga	Active Gα	0	k_{i1}	$2.51 \times 10^{-5}\mu m^2 s^{-1}$ (*10*)
Gd	Inactive Gα	0	D	$0.001\mu m^2 s^{-1}$ (*66*)
Gbg	Gβγ	0	k_{bp0}	0; $5.8 \times 10^{-3} s^{-1}$; $5.8 \times 10^{-3} s^{-1}$
GbgP	$G\beta^P\gamma$	0	k_{bpd}	0; $1 \times 0^{-3} s^{-1}$; $1 \times 10^{-3} s^{-1}$
Yck	Yck1/2	[b]4,000/sa	k_{bp1}	0; 0; $1 \times 10^{-5}\mu m^2 s^{-1}$
YckGbgP	Yck1/2-$G\beta^P\gamma$ complex	0	k_{bp2}	0; 0; $1 \times 10^{-7}\mu m^4 s^{-1}$
Fus3	Inactive Fus3	[c]2,130/v	k_{yi}	0; $5 \times 10^{-3}\mu m^2\ s^{-1}$; $5 \times 10^{-3}\ \mu m^2 s^{-1}$
Fus3P	Active Fus3	0	k_{ya}	0; $3 \times 10^{-3}\ s^{-1}$; $3 \times 10^{-3} s^{-1}$
			k_{fa}	0; 0; [d]$3\ \mu m^2 s^{-1}$
			k_{fd}	0; 0; $1\ s^{-1}$ (*67*)

Table S4: Definitions & Parameters. [a]Rate constants from Table S8. [b]The total number of Yck molecules per cell was reported to be 7,790 (*68*). We assumed 4,000 on the cell surface. [c]The total number of Fus3 molecules per cell was reported to be 8,480 (*68*), with about 25% in the cytoplasm (*67*). [d]We set Fus3 phosphorylation at 3X faster than its dephosphorylation based on Maeder et al. (*67*). Parameter values are color-coded according to network. Those in black are used in all three networks. Blue values correspond specifically to network 1, while those in green and red correspond to networks 2 and 3, respectively.

Rx #	Reaction	Comments
1	$\emptyset \xrightarrow{k_{rs}} \mathrm{R}$	Synthesis of pheromone receptor
2	$\mathrm{R} + \mathrm{L} \underset{k_{rlm}}{\overset{k_{rl}}{\rightleftharpoons}} \mathrm{RL}$	Association/disassociation of receptor & pheromone
3	$\emptyset \xrightarrow{k_{gs}} \mathrm{G}$	Synthesis of heterotrimeric G protein
4	$\mathrm{RL} + \mathrm{G} \xrightarrow{k_{ga}} \mathrm{RL} + \mathrm{Ga} + \mathrm{Gbg}$	Activation of G protein by liganded-receptor
5	$\mathrm{Ga} \xrightarrow{k_{gad}} \mathrm{Gd}$	Inactivation of Gα
6	$\mathrm{Gd} + \mathrm{Gbg} \xrightarrow{k_{gd}} \mathrm{G}$	Reassociation of Gα & Gβγ to form the heterotrimer
7	$\mathrm{Yck} + \mathrm{R} + (\mathrm{G}) \xrightarrow{k_{i0}} \mathrm{Yck}$	Yck1/2-stimulated internalization of inactive receptors and heterotrimeric G protein[a]
8	$\mathrm{Yck} + \mathrm{RL} + (\mathrm{G}) \xrightarrow{k_{i1}} \mathrm{Yck}$	Yck1/2-stimulated internalization of active receptors and heterotrimeric G protein[a]
9	$\mathrm{Gbg} \underset{k_{bpd}}{\overset{k_{bp0}}{\rightleftharpoons}} \mathrm{GbgP}$	Phosphorylation and dephosphorylation of Gβγ
10	$\mathrm{GbgP} + \mathrm{Yck} \underset{k_{ya}}{\overset{k_{yi}}{\rightleftharpoons}} \mathrm{YckGb}$	Association/disassociation of $G\beta^{P}\gamma$ and Yck1
11	$\mathrm{GbgP} + \mathrm{Fus3} \xrightarrow{k_{fa}} \mathrm{GbgP} + \mathrm{Fus3A}$	Activation of Fus3 by $G\beta^{P}\gamma$
12	$\mathrm{Fus3A} \xrightarrow{k_{fd}} \mathrm{Fus3}$	Deactivation of Fus3
13	$\mathrm{Fus3A} + \mathrm{Gbg} \xrightarrow{k_{bp1}} \mathrm{Fus3A} + \mathrm{GbgP}$	Phosphorylation of Gβ by active Fus3
14	$\mathrm{Ga} + \mathrm{Fus3A} + \mathrm{Gbg} \xrightarrow{k_{bp2}} \mathrm{Ga} + \mathrm{Fus3A} + \mathrm{GbgP}$	Gα recruitment of active Fus3 to phosphorylate Gβ

Table S5. Reaction formulae. [a]The stoichiometry of the internalized receptor and heterotrimeric G protein is assumed to be 1:1.

Eq #	Equation
1	$\frac{\partial[\mathrm{R}]}{\partial t} = D\nabla^2[\mathrm{R}] + k_{rs} - k_{rl}[\mathrm{R}][\mathrm{L}] + k_{rlm}[\mathrm{RL}] - k_{i0}[\mathrm{Yck}][\mathrm{R}]$
2	$\frac{\partial[\mathrm{RL}]}{\partial t} = D\nabla^2[\mathrm{RL}] + k_{rl}[\mathrm{R}][\mathrm{L}] - k_{rlm}[\mathrm{RL}] - k_{i1}[\mathrm{Yck}][\mathrm{RL}]$
3	$gr0 = \min(1, [G]/[R])$
4	$gr1 = \min(1, [G]/[RL])$
5	$\frac{\partial[\mathrm{G}]}{\partial t} = D\nabla^2[\mathrm{G}] + k_{gs} + k_{gd}[\mathrm{Gd}][\mathrm{Gbg}] - k_{ga}[\mathrm{G}][\mathrm{RL}] - k_{i0} \cdot gr0[\mathrm{Yck}][R] - k_{i1} \cdot gr1[\mathrm{Yck}][\mathrm{RL}]$
6	$\frac{\partial[\mathrm{Ga}]}{\partial t} = D\nabla^2[\mathrm{Ga}] + k_{ga}[\mathrm{G}][\mathrm{RL}] - k_{gad}[\mathrm{Ga}]$
7	$\frac{\partial[\mathrm{Gd}]}{\partial t} = D\nabla^2[\mathrm{Gd}] + k_{gad}[\mathrm{Ga}] - k_{gd}[\mathrm{Gd}][\mathrm{Gbg}]$
8	$\frac{\partial[\mathrm{Gbg}]}{\partial t} = D\nabla^2[\mathrm{Gbg}] + k_{ga}[\mathrm{G}][\mathrm{RL}] - k_{gd}[\mathrm{Gd}][\mathrm{Gbg}] + k_{bpd}[\mathrm{GbgP}] - k_{bp0}[\mathrm{Gbg}] - k_{bp1}[\mathrm{Fus3A}][\mathrm{Gbg}] - k_{bp2}[\mathrm{Ga}][\mathrm{Fus3A}][\mathrm{Gbg}]$
9	$\frac{\partial[\mathrm{GbgP}]}{\partial t} = D\nabla^2[\mathrm{GbgP}] - k_{bpd}[\mathrm{GbgP}] + k_{bp0}[\mathrm{Gbg}] + k_{bp1}[\mathrm{Fus3A}][\mathrm{Gbg}] + k_{bp2}[\mathrm{Ga}][\mathrm{Fus3A}][\mathrm{Gbg}] - k_{yi}[\mathrm{Yck}][\mathrm{GbgP}] + k_{ya}[\mathrm{YckGbgP}]$
10	$\frac{\partial[\mathrm{Yck}]}{\partial t} = D\nabla^2[\mathrm{Yck}] - k_{yi}[\mathrm{Yck}][\mathrm{GbgP}] + k_{ya}[\mathrm{YckGbgP}]$
11	$\frac{\partial[\mathrm{YckGbgP}]}{\partial t} = D\nabla^2[\mathrm{YckGbgP}] + k_{yi}[\mathrm{Yck}][\mathrm{GbgP}] - k_{ya}[\mathrm{YckGbgP}]$
12	$\frac{\partial[\mathrm{Fus3}]}{\partial t} = D\nabla^2[\mathrm{Fus3}] + k_{fd}[\mathrm{Fus3A}] - k_{fa}[\mathrm{GbgP}][\mathrm{Fus3}]$
13	$\frac{\partial[\mathrm{Fus3A}]}{\partial t} = D\nabla^2[\mathrm{Fus3A}] - k_{fd}[\mathrm{Fus3A}] + k_{fa}[\mathrm{GbgP}][\mathrm{Fus3}]$

Table S6. Partial Differential Equations

Fig. 1

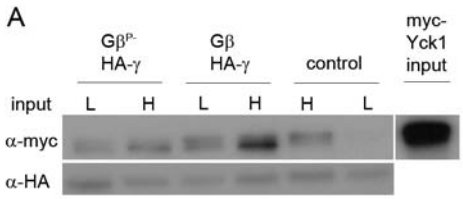

B

Affinity Beads	AI	SAN	Gβ/Gβ^{P-} ratio
Gβγ	4.46E+04	4.03E+04	2.08
Gβ^{P-}γ	2.37E+04	1.93E+04	
Empty	4.33E+03	-	

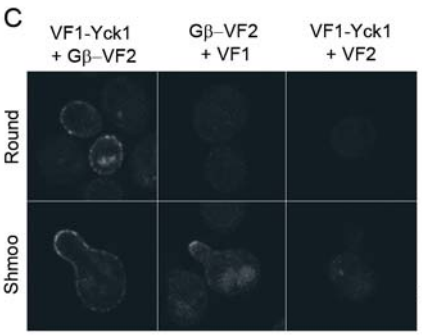

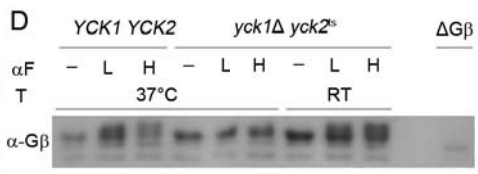

Fig. 2

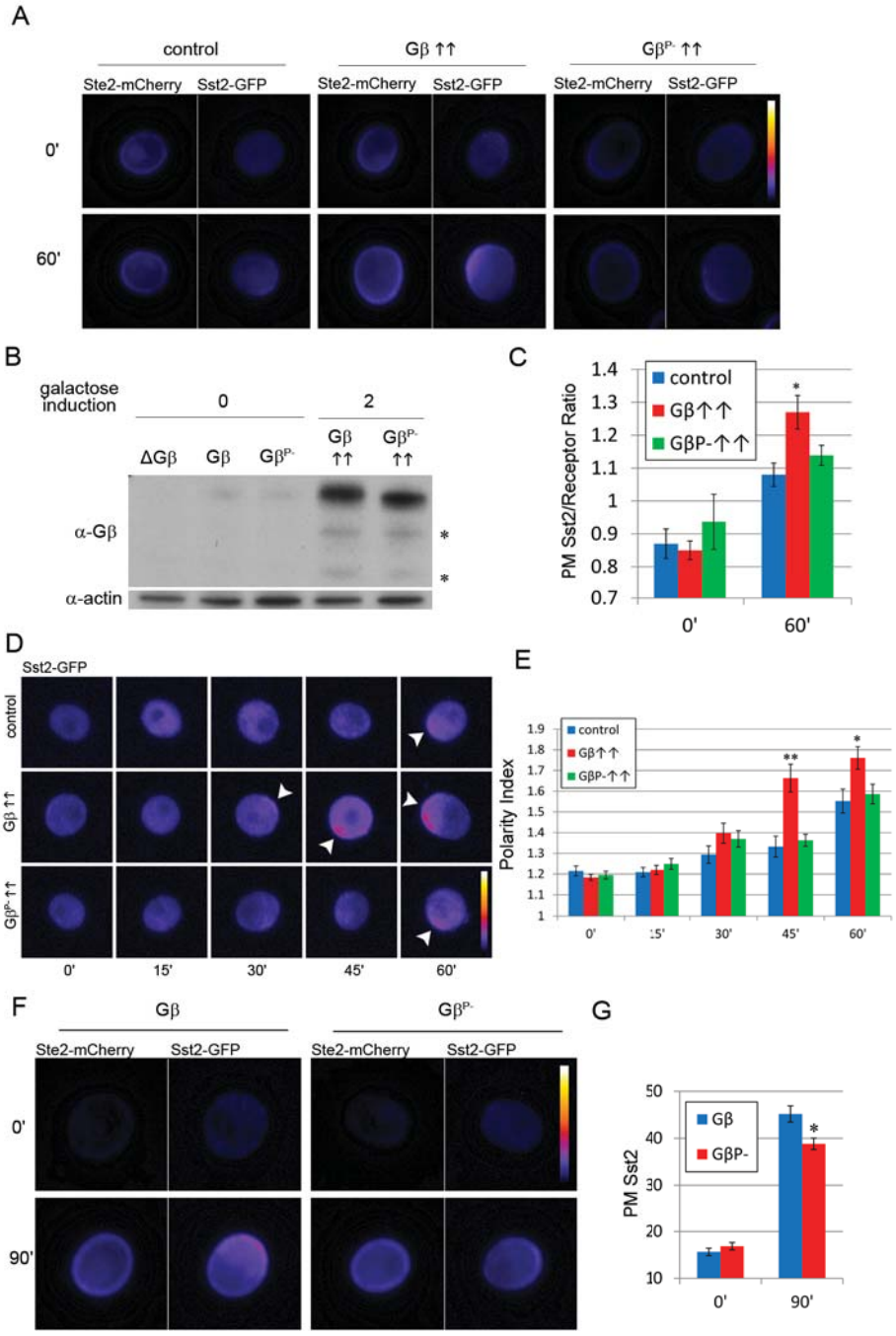
A
control
Gβ ↑↑
Gβ^P- ↑↑
Ste2-mCherry
Sst2-GFP
0'
60'
B
galactose induction
0
2
ΔGβ
Gβ
Gβ^P-
Gβ ↑↑
Gβ^P- ↑↑
α-Gβ
α-actin
*
C
PM Sst2/Receptor Ratio
control
Gβ↑↑
GβP-↑↑
1.4
1.3
1.2
1.1
1
0.9
0.8
0.7
0'
60'
D
Sst2-GFP
control
Gβ ↑↑
Gβ^P- ↑↑
0'
15'
30'
45'
60'
E
Polarity Index
control
Gβ↑↑
GβP-↑↑
1.9
1.8
1.7
1.6
1.5
1.4
1.3
1.2
1.1
1
0'
:5'
30'
45'
60'
**
*
F
Gβ
Gβ^P-
Ste2-mCherry
Sst2-GFP
0'
90'
G
PM Sst2
Gβ
GβP-
50
40
30
20
10
0'
90'
*

Fig. 3

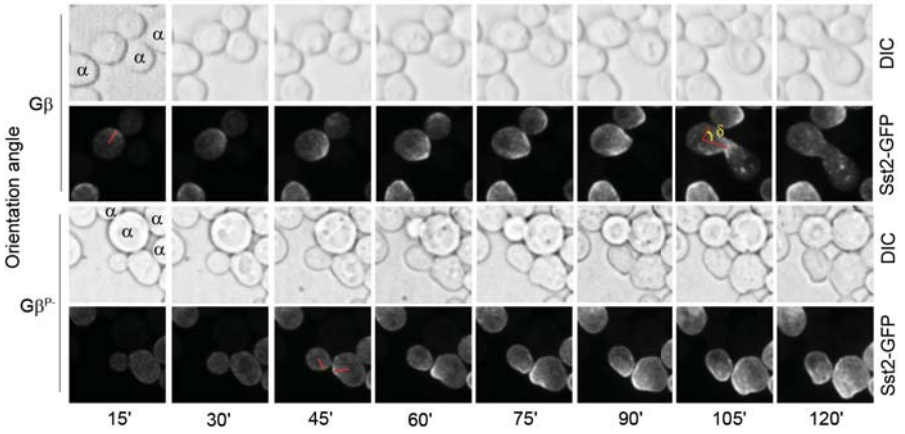
Orientation angle
Gβ
Gβ^P-
DIC
Sst2-GFP
DIC
Sst2-GFP
α
15'
30'
45'
60'
75'
90'
105'
120'

Fig. 4

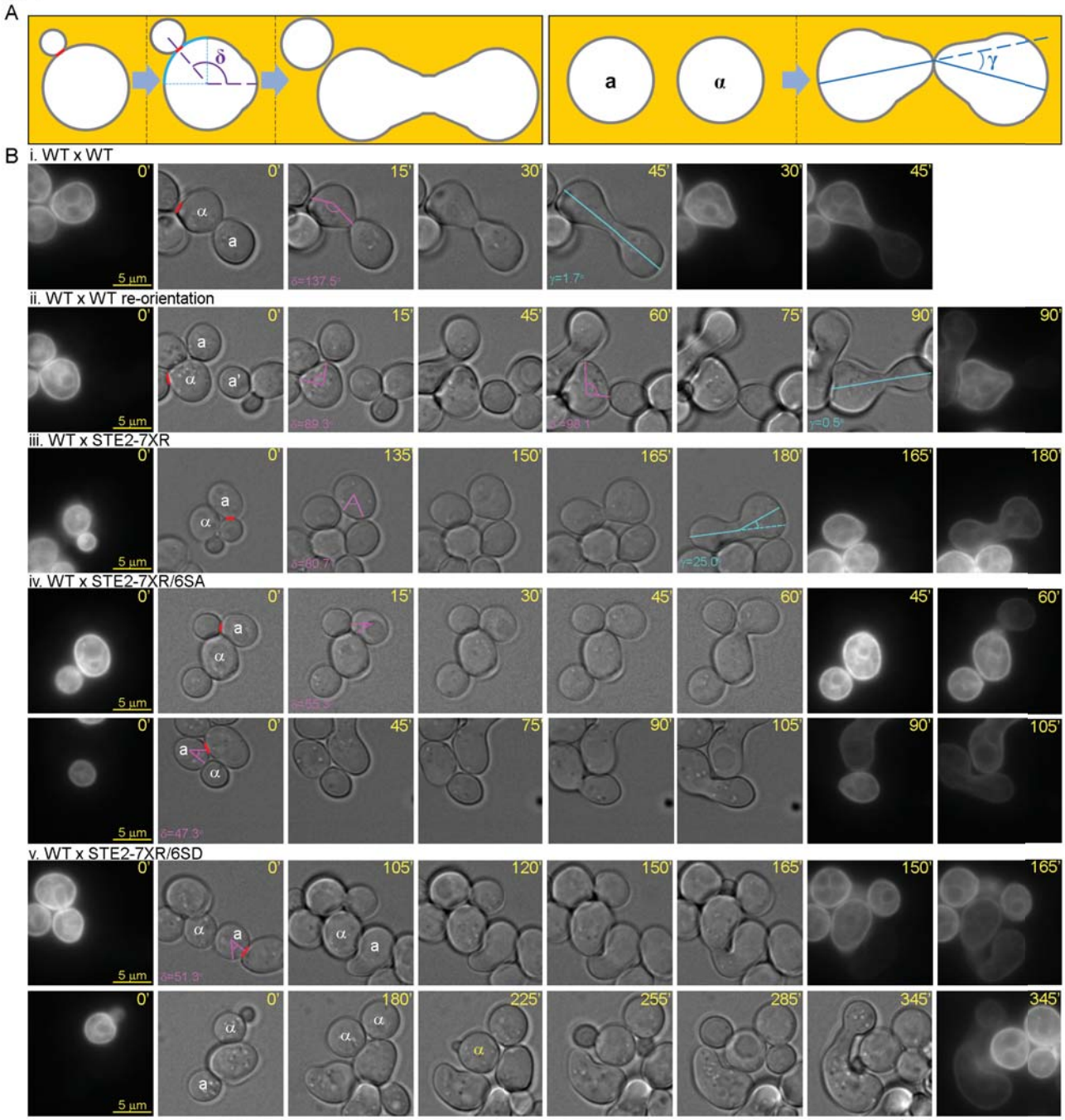
A
δ
a
α
γ
B
i. WT x WT
ii. WT x WT re-orientation
iii. WT x STE2-7XR
iv. WT x STE2-7XR/6SA
v. WT x STE2-7XR/6SD
5 μm

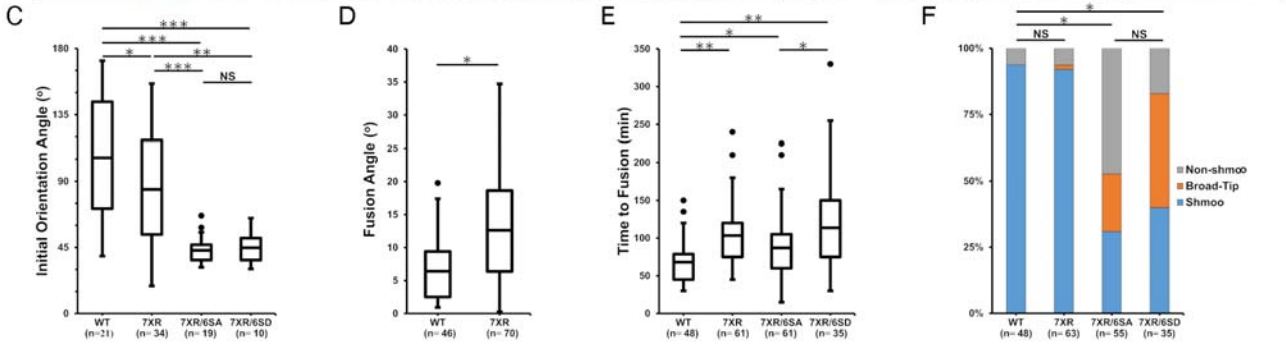
C
Initial Orientation Angle (°)
WT (n=21)
7XR (n=34)
7XR/6SA (n=19)
7XR/6SD (n=10)
D
Fusion Angle (°)
WT (n=46)
7XR (n=70)
E
Time to Fusion (min)
WT (n=48)
7XR (n=61)
7XR/6SA (n=61)
7XR/6SD (n=35)
F
WT (n=48)
7XR (n=63)
7XR/6SA (n=55)
7XR/6SD (n=35)
Non-shmoo
Broad-Tip
Shmoo

Fig. 5

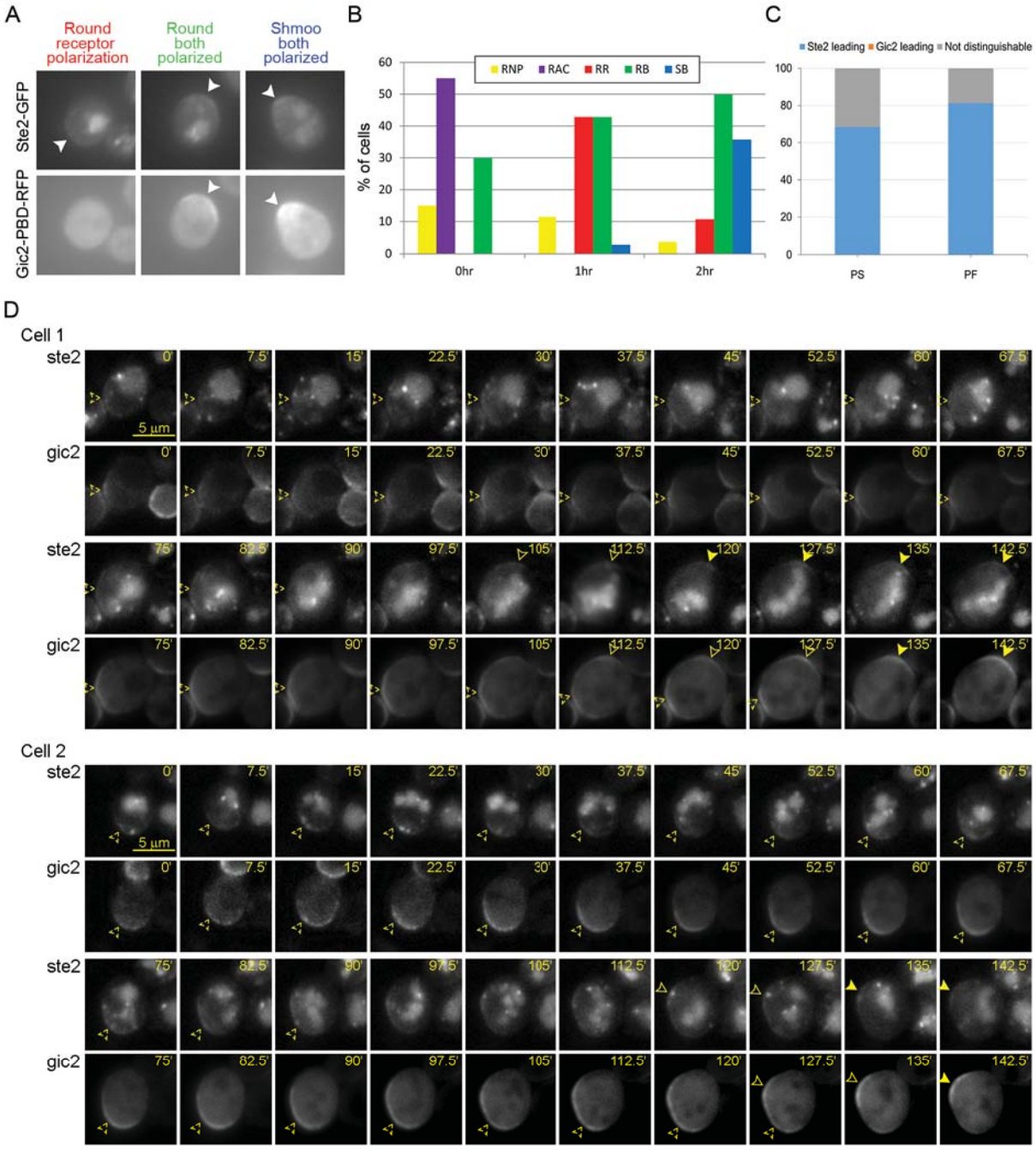
A
Round receptor polarization
Round both polarized
Shmoo both polarized
Ste2-GFP
Gic2-PBD-RFP
B
RNP
RAC
RR
RB
SB
% of cells
0hr
1hr
2hr
C
Ste2 leading
Gic2 leading
Not distinguishable
PS
PF
D
Cell 1
Cell 2
ste2
gic2
5 μm

Fig. 6

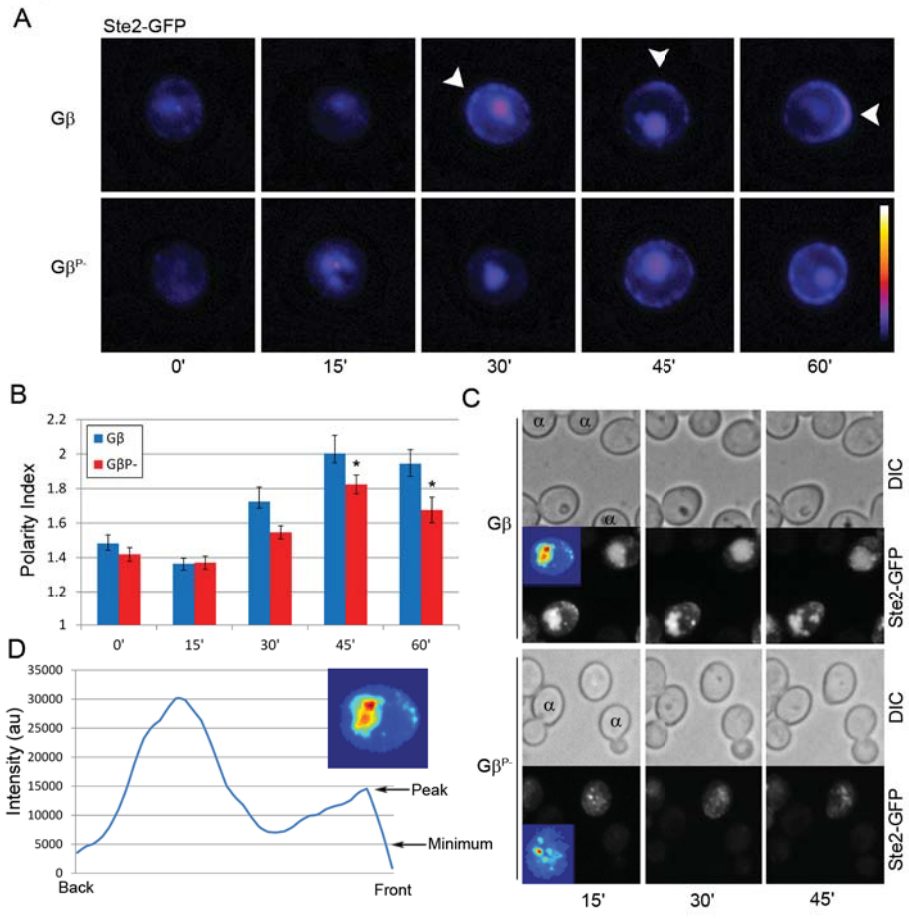
A
Ste2-GFP
Gβ
Gβ^P-
0'
15'
30'
45'
60'
B
Gβ
GβP-
Polarity Index
2.2
2
1.8
1.6
1.4
1.2
1
0'
15'
30'
45'
60'
C
Gβ
Gβ^P-
DIC
Ste2-GFP
α
15'
30'
45'
D
Intensity (au)
35000
30000
25000
20000
15000
10000
5000
0
Peak
Minimum
Back
Front

Fig. 7

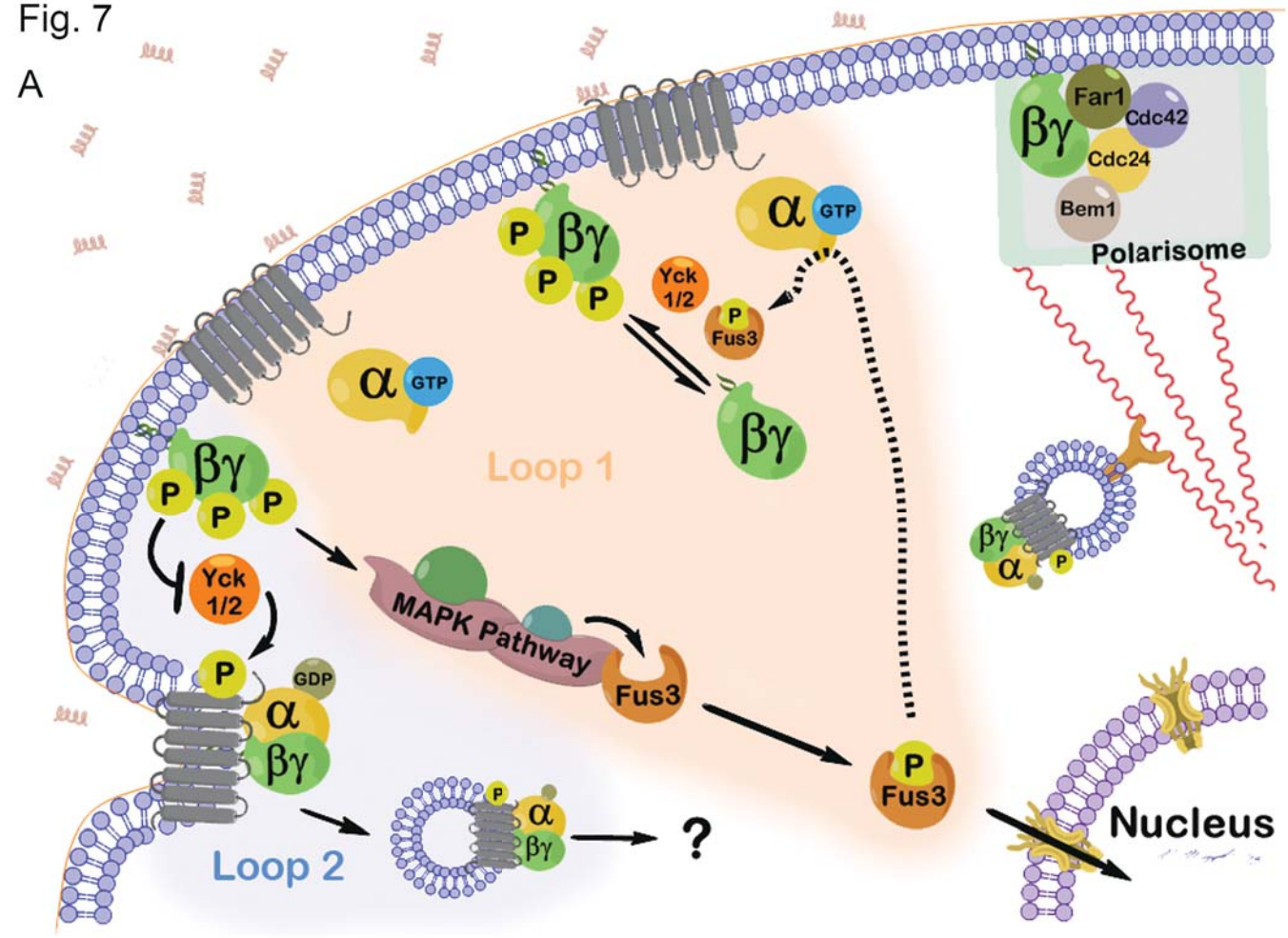
A
Far1
Cdc42
Cdc24
Bem1
Polarisome
GTP
Yck 1/2
P
Fus3
Loop 1
MAPK Pathway
GDP
Loop 2
?
Nucleus

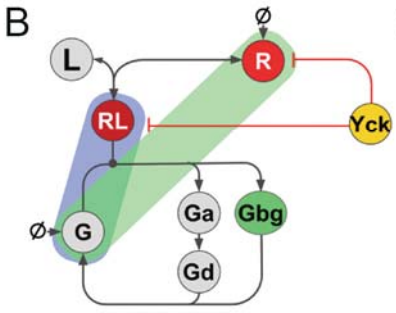
B
L
R
RL
Yck
G
Ga
Gbg
Gd

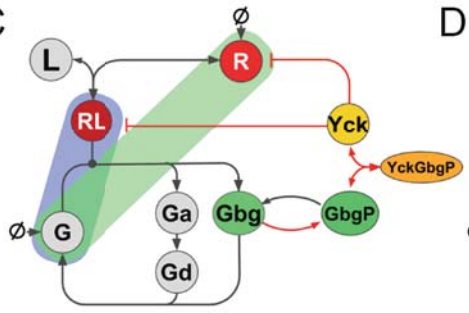
C
L
R
RL
Yck
YckGbgP
G
Ga
Gbg
GbgP
Gd

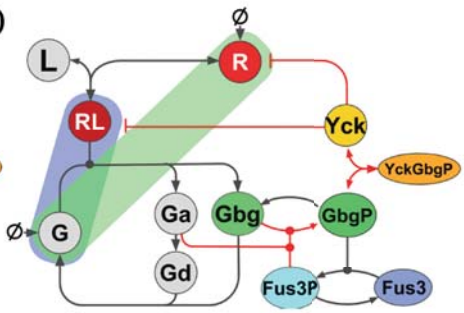
D
L
R
RL
Yck
YckGbgP
G
Ga
Gbg
GbgP
Gd
Fus3P
Fus3

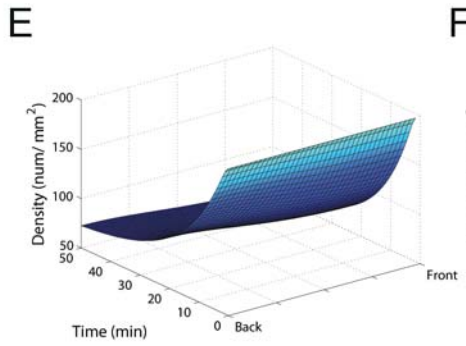
E
Density (num/ mm2)
Time (min)
Front
Back

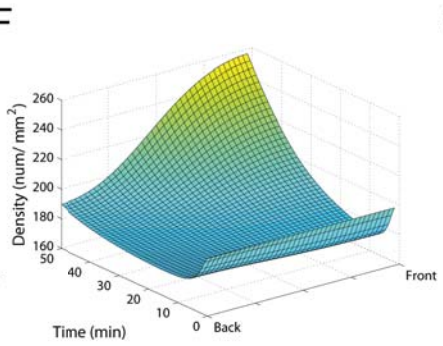
F
Density (num/ mm2)
Time (min)
Front
Back

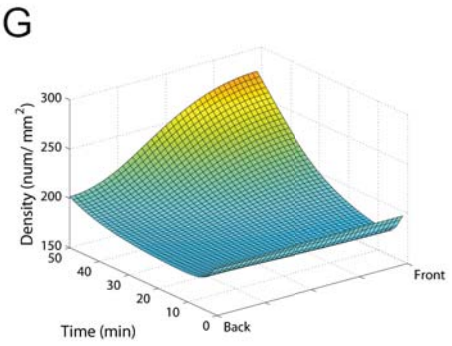
G
Density (num/ mm2)
Time (min)
Front
Back

Fig. S1

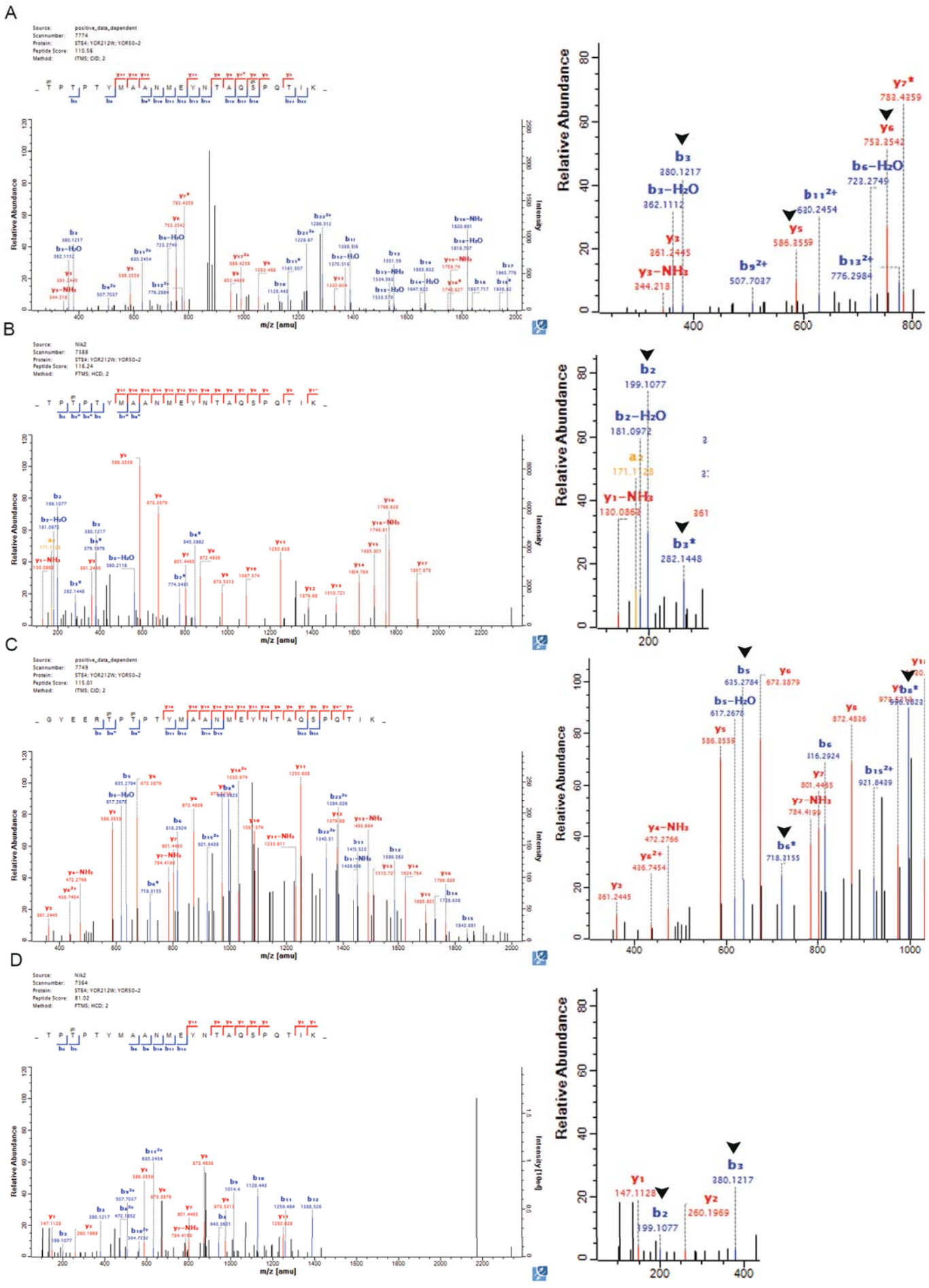

Fig. S2

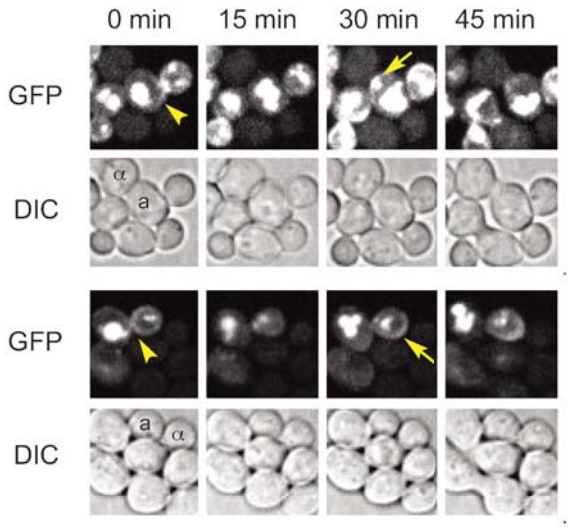

Fig. S3

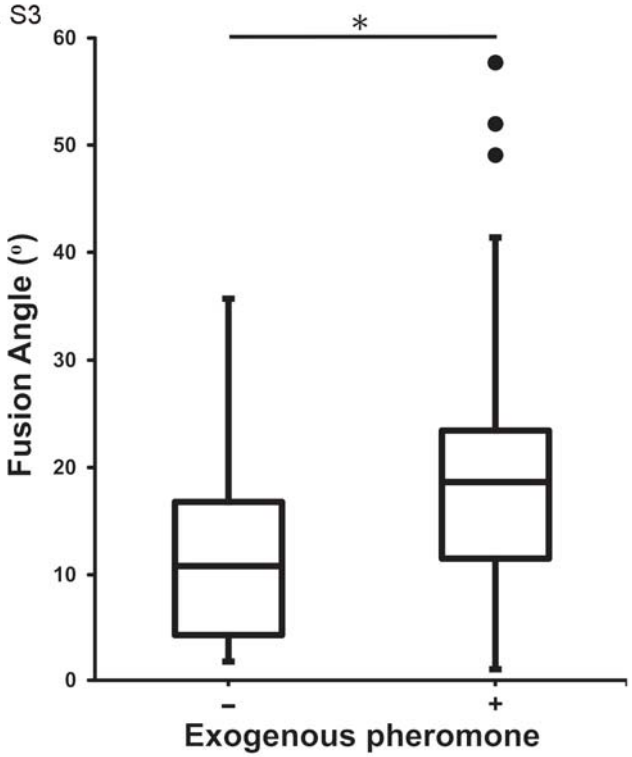

Fig. S4

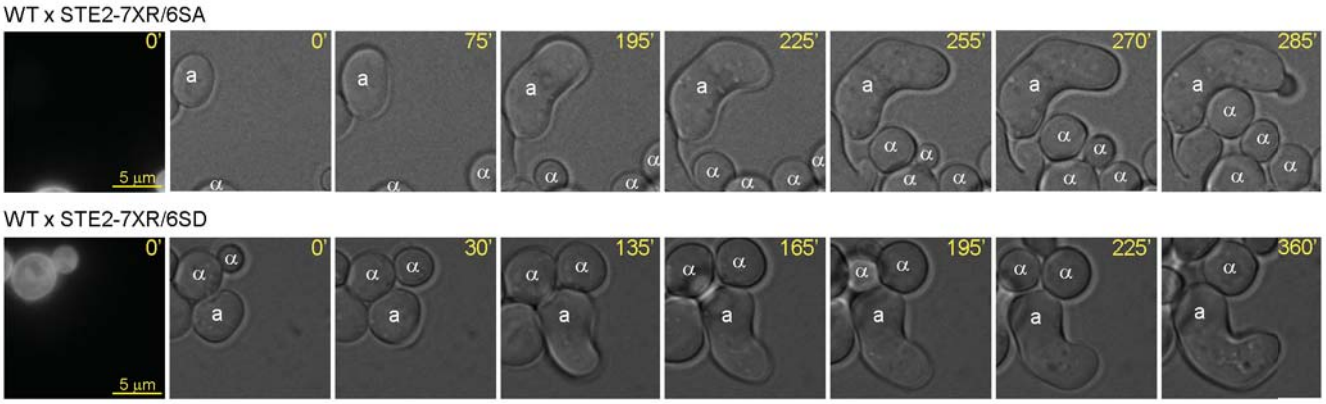
A
WT x STE2-7XR/6SA
0'
0'
75'
195'
225'
255'
270'
285'
5 µm
B
WT x STE2-7XR/6SD
0'
0'
30'
135'
165'
195'
225'
360'
5 µm

Fig. S5

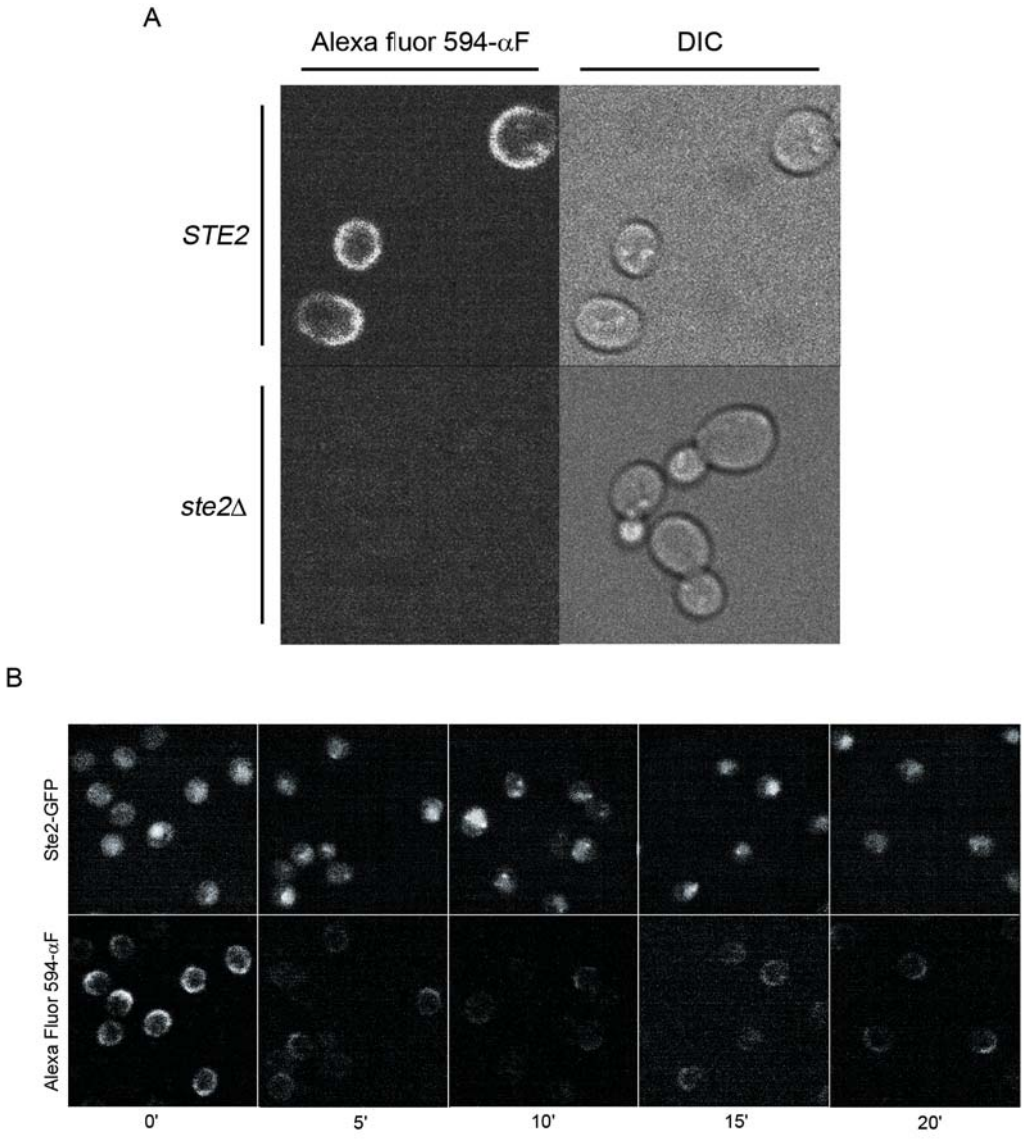
A
Alexa fluor 594-αF
DIC
STE2
ste2Δ
B
Ste2-GFP
Alexa Fluor 594-αF
0'
5'
10'
15'
20'

Fig. S6

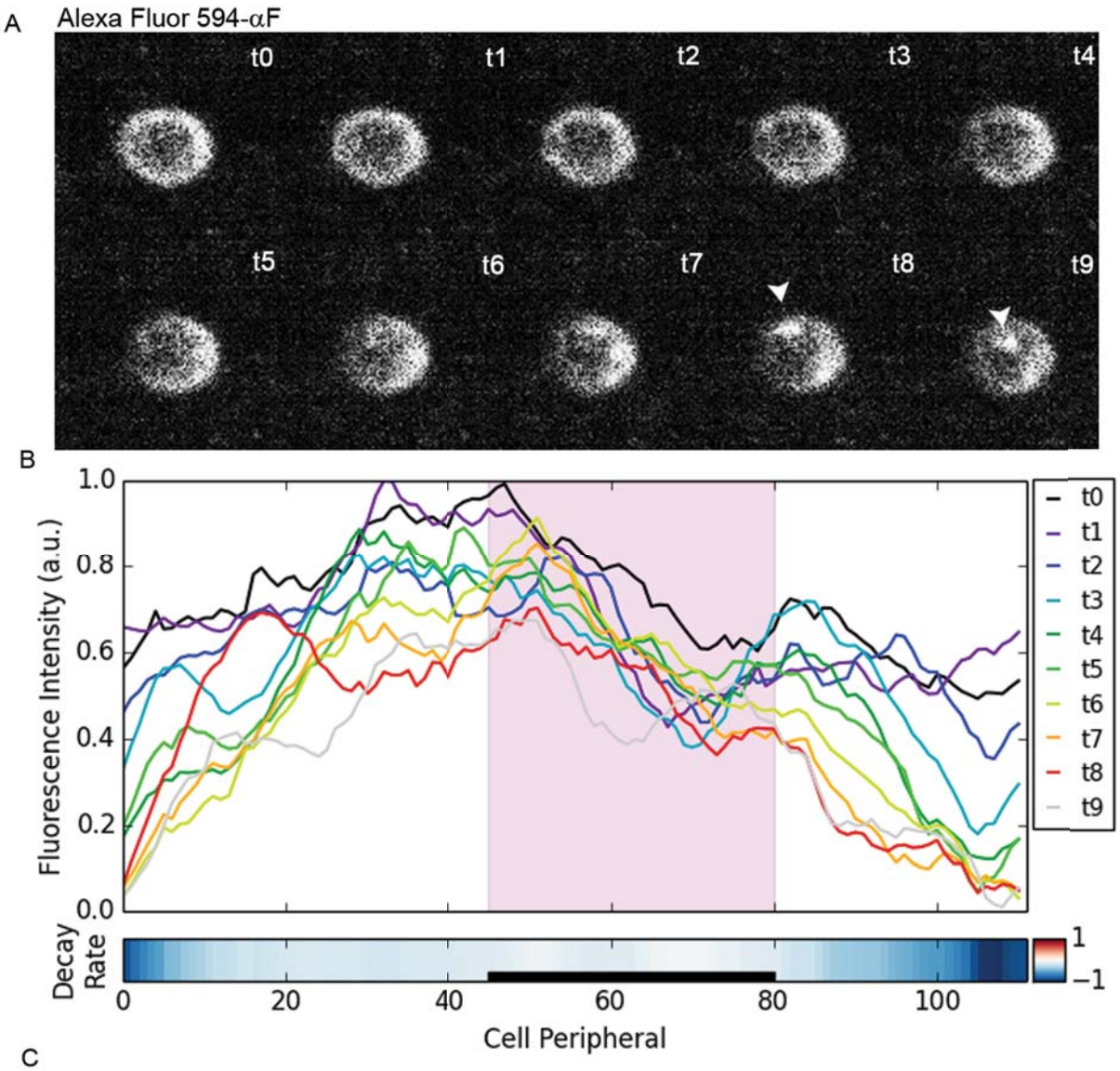
A
Alexa Fluor 594-αF
t0
t1
t2
t3
t4
t5
t6
t7
t8
t9
B
Fluorescence Intensity (a.u.)
1.0
0.8
0.6
0.4
0.2
0.0
t0
t1
t2
t3
t4
t5
t6
t7
t8
t9
Decay Rate
1
−1
0
20
40
60
80
100
Cell Peripheral
C
Relative Fluorescence Intensity (a.u.)
1.4
1.2
1.0
0.8
0.6
0.4
0.2
0.0
Protected
Unprotected
0
2
4
6
8
Time Point

Fig. S7

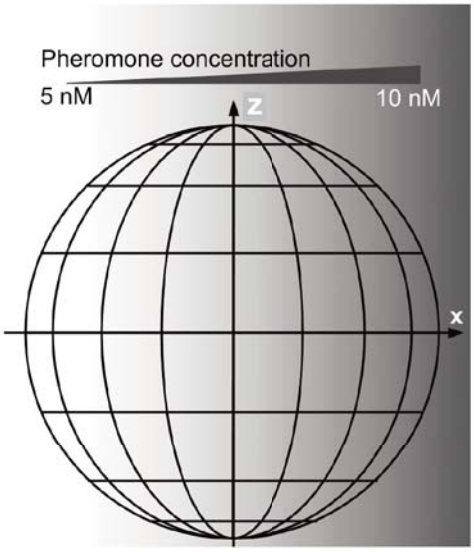

Fig. S8

A

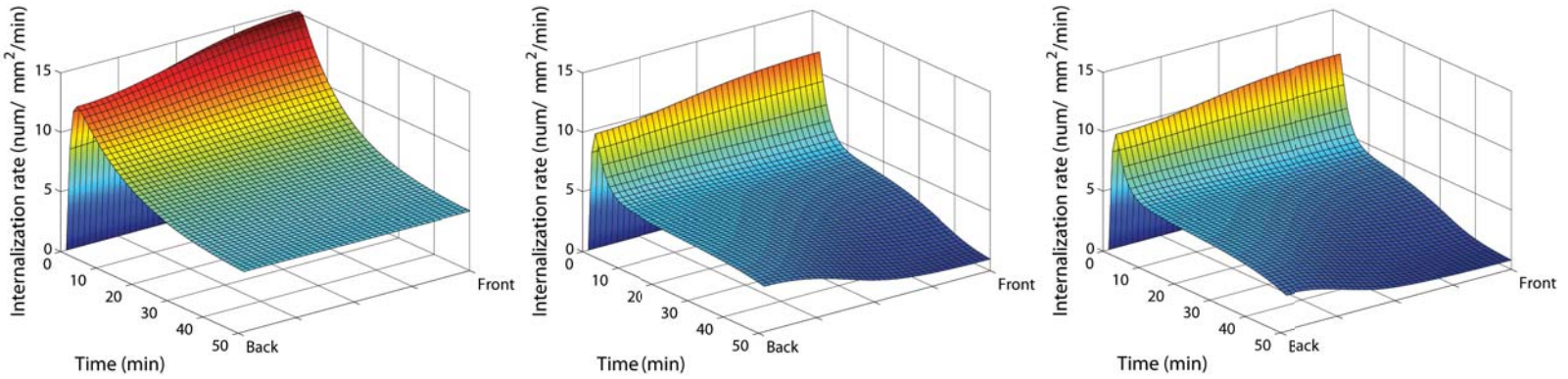
Internalization rate (num/ mm 2 /min)
15
10
5
0
0
10
20
30
40
50
Time (min)
Back
Front
Internalization rate (num/ mm 2 /min)
15
10
5
0
0
10
20
30
40
50
Time (min)
Back
Front
Internalization rate (num/ mm 2 /min)
15
10
5
0
0
10
20
30
40
50
Time (min)
Back
Front

B

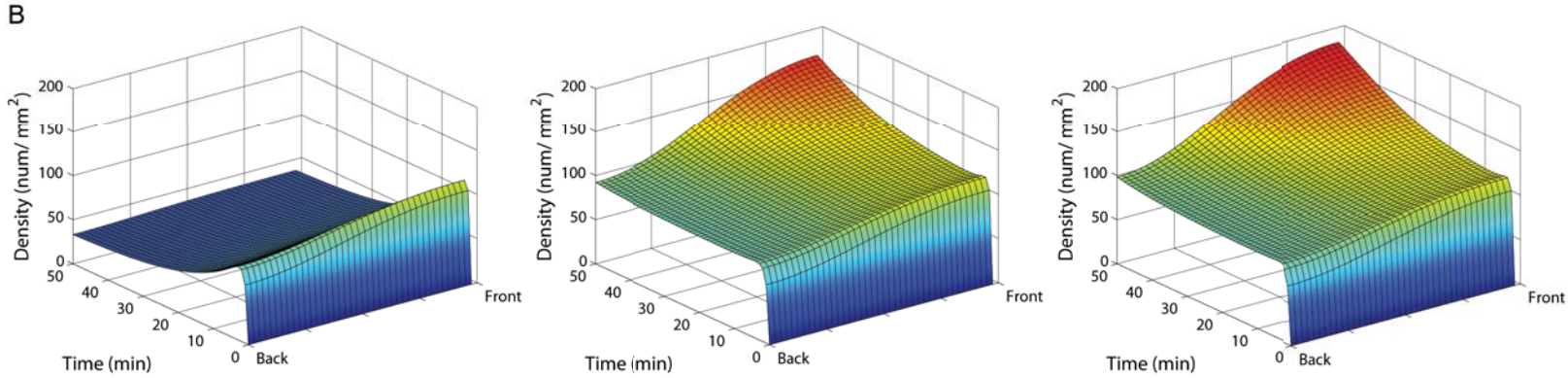
Density (num/ mm 2)
200
150
100
50
0
50
40
30
20
10
0
Time (min)
Back
Front
Density (num/ mm 2)
200
150
100
50
0
50
40
30
20
10
0
Time (min)
Back
Front
Density (num/ mm 2)
200
150
100
50
0
50
40
30
20
10
0
Time (min)
Back
Front

Fig. S9

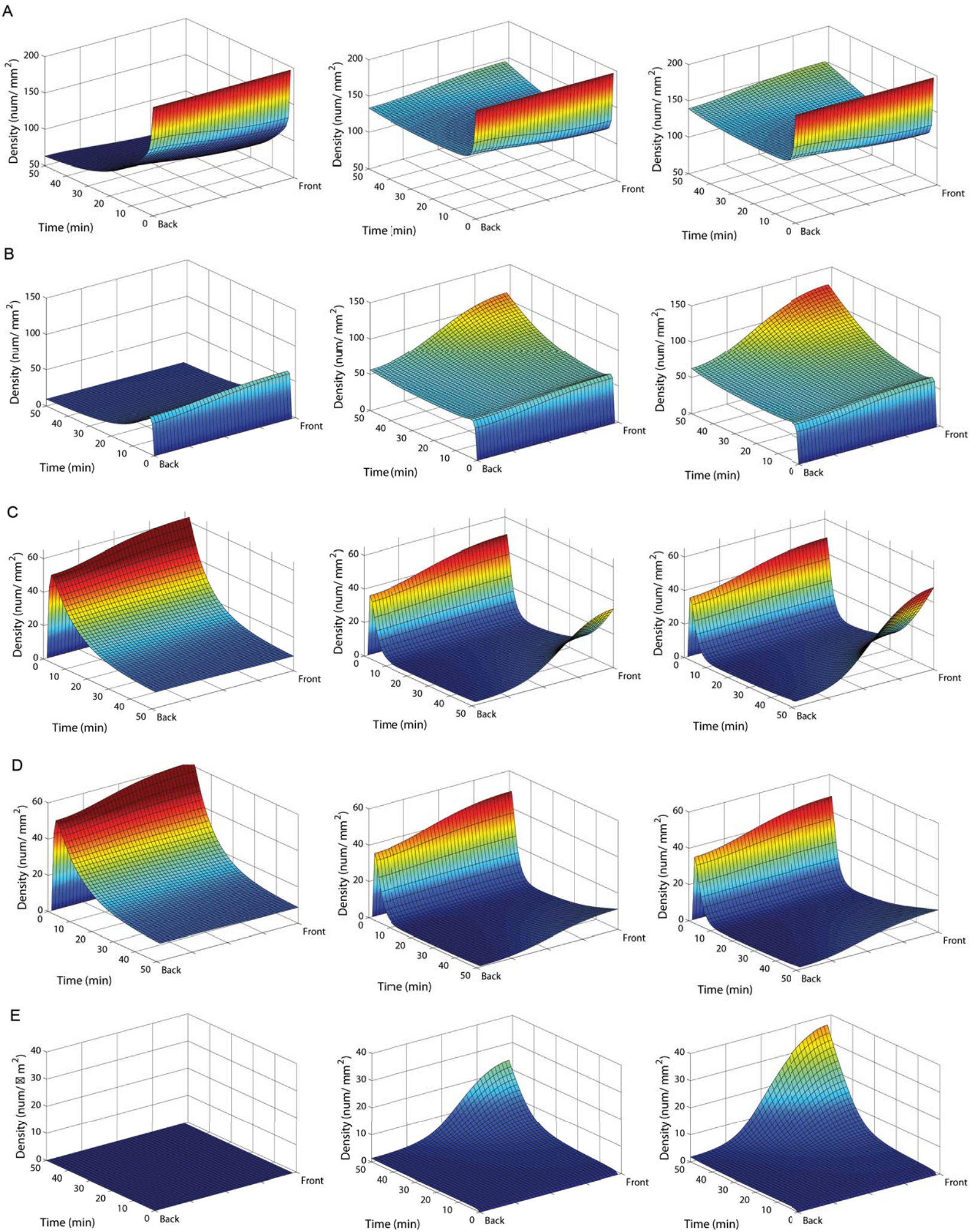

Fig. S10

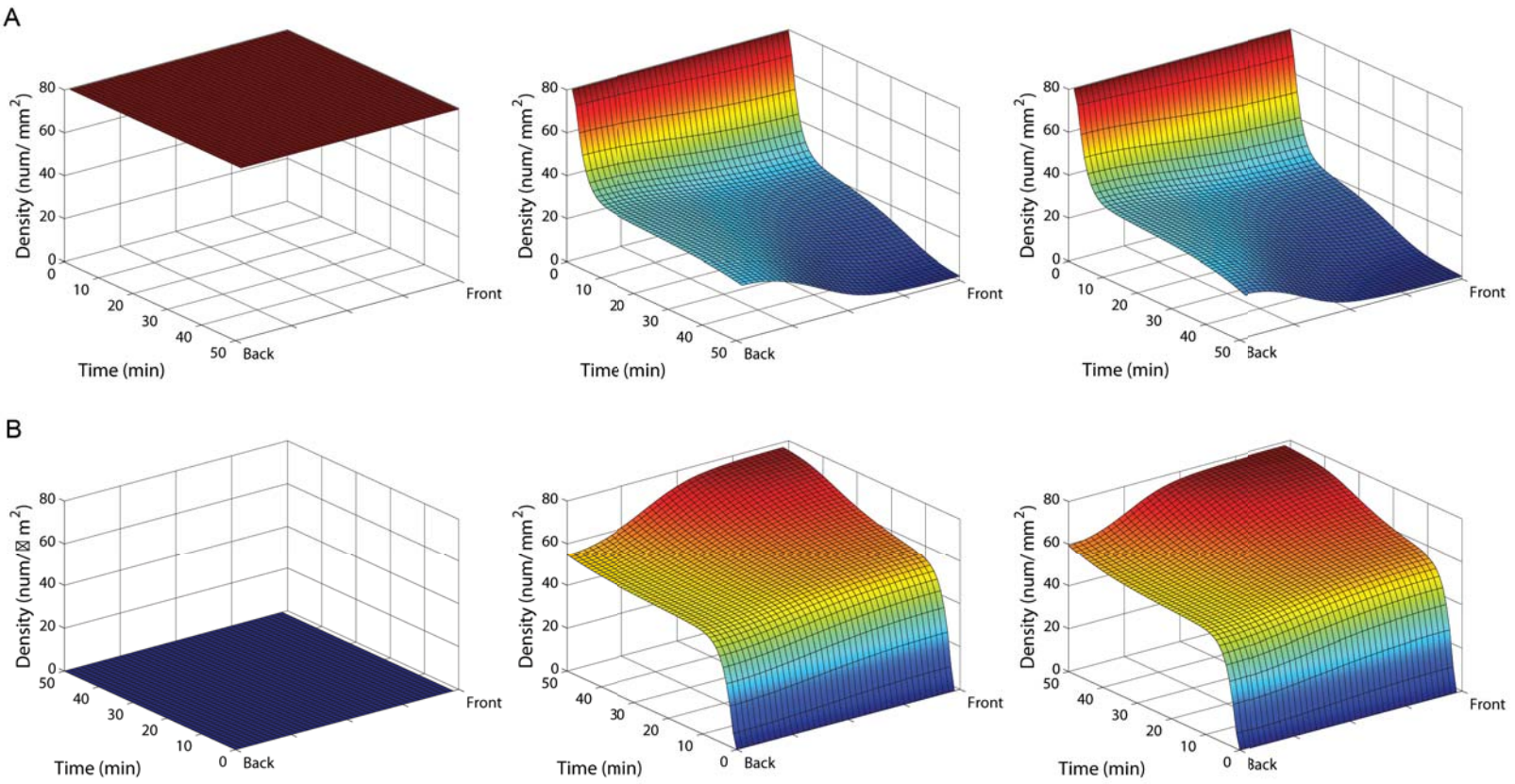
A
Density (num/ mm2)
0
20
40
60
80
Time (min)
0
10
20
30
40
50
Front
Back
B
Density (num/ mm2)
Time (min)
Front
Back